INL/EXT-17-43609
Revision 0

Advanced Reactor Technologies (ART): Very High Temperature Reactor (VHTR) Research and Development (R&D) Quarterly Report

July, August, and September 2017

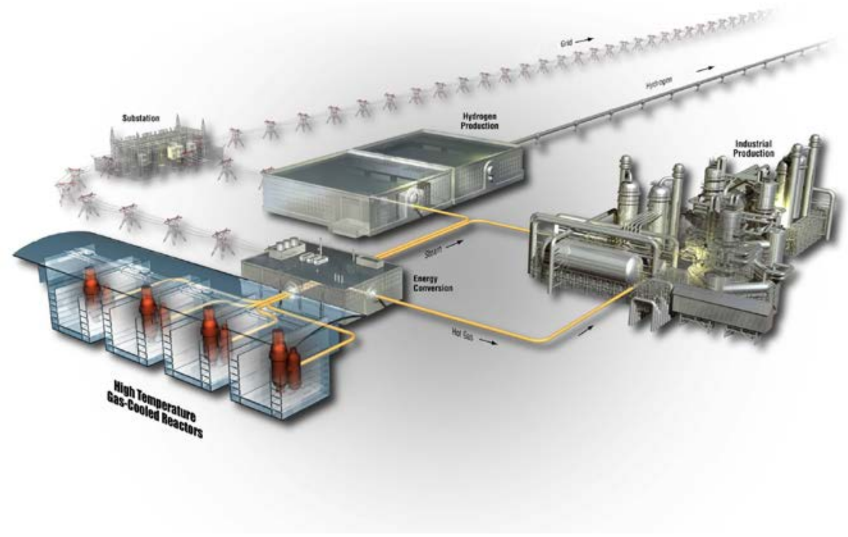

Please note this report contains preliminary data, interim conclusions and observations from work-in-progress.

The INL is a
U.S. Department of Energy
National Laboratory
operated by
Battelle Energy Alliance

Idaho National Laboratory

DISCLAIMER

This information was prepared as an account of work sponsored by an agency of the U.S. Government. Neither the U.S. Government nor any agency thereof, nor any of their employees, makes any warranty, expressed or implied, or assumes any legal liability or responsibility for the accuracy, completeness, or usefulness of any information, apparatus, product, or process disclosed, or represents that its use would not infringe privately owned rights. References herein to any specific commercial product, process, or service by trade name, trade mark, manufacturer, or otherwise does not necessarily constitute or imply its endorsement, recommendation, or favoring by the U.S. Government or any agency thereof. The views and opinions of authors expressed herein do not necessarily state or reflect those of the U.S. Government or any agency thereof.

INL/EXT-17-43609
Revision 0

Advanced Reactor Technologies (ART): Very High Temperature Reactor (VHTR) Research and Development (R&D) Quarterly Report

July, August, and September 2017

Idaho National Laboratory
INL ART TDO Program
Idaho Falls, Idaho 83415

http://www.inl.gov

Prepared for the
U.S. Department of Energy
Office of Nuclear Energy
Under DOE Idaho Operations Office
Contract DE-AC07-05ID14517

INL ART Program

Advanced Reactor Technologies (ART): Very High Temperature Reactor (VHTR) Research and Development (R&D) Quarterly Report

INL/EXT-17-43609
Revision 0

July, August, and September 2017

Approved by:

Diane V C

Diane V. Croson
INL ART TDO Deputy Director

11/13/17
Date

CONTENTS

FIGURES

TABLES

ACRONYMS

AGC	advanced graphite creep
AGR	Advanced Gas Reactor
ASME	American Society of Mechanical Engineers
ASTM	American Society of Testing and Materials
ATR	Advanced Test Reactor
BP	burnable poison
BWXT	BWX Technologies
CCCTF	Core Conduction Cooldown Test Facility
CRP	Coordinated Research Project
DC	direct current
DH	double heterogeneity
DLBL	deconsolidation-leach-burn-leach
DOE	Department of Energy
DTF	designed-to-fail
EDS	energy dispersive spectroscopy
EOI	end of irradiation
FACS	fuel accident condition simulator
FIMA	fissions per initial metal atom
FY	fiscal year
GA	General Atomics
GIF	Generation IV International Forum
GRS	Gesellschaft für Anlagen- und Reaktorsicherheit
HFEF	Hot Fuel Examination Facility
HOG	HFEF out-of-cell gamma
HTGR	high-temperature gas-cooled reactor
HTTF	High Temperature Test Facility
HTV	high-temperature vessel
IAEA	International Atomic Energy Agency
ILS	inter-laboratory study
IMGA	irradiated microsphere gamma analyzer
INGSM	International Nuclear Graphite Specialists Meeting
INL	Idaho National Laboratory
IPyC	inner pyrolytic carbon

KAERI	Korea Atomic Energy Research Institute
KI	Kurchatov Institute
LBL	leach-burn-leach
LWR	light-water reactor
MHTGR	modular high-temperature gas-cooled reactor
NDMAS	Nuclear Data Management and Analysis System
NEA	Nuclear Energy Agency
NRAD	Neutron Radiography Reactor
NWU	North West University
OECD	Organization for Economic Cooperation and Development
OPyC	outer pyrolytic carbon
ORNL	Oak Ridge National Laboratory
OSU	Oregon State University
PED	precession electron diffraction
PIE	post-irradiation examination
PNNL	Pacific Northwest National Laboratory
PyC	pyrolytic carbon
R&D	research and development
SCALE	Standardized Computer Analyses for Licensing Evaluation
SEM	scanning electron microscopy
SiC	silicon carbide
STEM	scanning transmission electron microscopy
TA	time averaged
TAVA	time averaged, volume averaged
TEM	transmission electron microscopy
TRISO	tristructural isotropic
UCO	uranium carbide/oxide
UO_2	uranium oxide
VHTRC	Very High Temperature Reactor Critical Assembly

Advanced Reactor Technologies (ART): Very High Temperature Reactor (VHTR) Research and Development (R&D) Quarterly Report

1. MAJOR ACCOMPLISHMENTS

1.1 Fuels Development

Highlights of Advanced Gas Reactor (AGR) fuels development activities during July through September 2017 are as follows:

July

- AGR-5/6/7 fuel compact characterization is mostly complete.
- Continued development of a residual uranium and government-furnished equipment disposition plan between BWX Technologies (BWXT) and Idaho National Laboratory (INL).
- Completed an x-ray computed tomography scan of an AGR-5/6/7 fuel compact with a 25% packing fraction.
- Completed radiochemical analysis of the Core Conduction Cooldown Test Facility (CCCTF) furnace internals and fission product release from a 1600°C safety test of AGR-2 uranium carbide/oxide (UCO) Compact 2-3-1.
- Completed 6-hour gamma scanning of randomly selected particles from 1600°C safety-tested UCO Compact 6-4-2 with the irradiated microsphere gamma analyzer (IMGA) and selected particles for x-ray tomography and materialographic examination.
- Initiated full IMGA survey of all tristructural isotropic (TRISO) particles deconsolidated from 1700°C safety-tested uranium oxide (UO_2) Compact 3-4-1; multiple particles show a reduced residual cesium inventory, as expected from the cesium release detected in the CCCTF.
- Completed deconsolidation and pre-burn-leach of as-irradiated AGR-2 UCO Compact 6-2-3.
- Completed shipment of four irradiated AGR-2 compacts (2-1-1, 5-2-1, 6-2-1, and 6-2-2) from INL to Oak Ridge National Laboratory (ORNL). This fulfills a Level 3 milestone to complete two AGR-2 compact shipments in fiscal year (FY) 2017.
- Completed tomographic gamma scans of the inner graphite rings from AGR-3/4 Capsules 4 and 5 using the precision gamma scanner.
- Completed physical sampling of inner and outer rings from AGR-3/4 Capsules 3 and 7.
- Prepared AGR-3/4 Capsule 5 and 8 inner and outer rings for physical sampling.
- Completed installation of mass-spectrometer/carbon monoxide analyzer for the air/moisture-ingress furnace development furnace.
- Completed installation of the furnace for irradiated TRISO-particle testing into a radiological hood in the ORNL 3525 hot cell building; demonstration of operation and final radiological work procedure development is in progress.
- Continued oxidation testing of graphite matrix-only samples.
- Completed anisotropy and defective inner pyrolytic carbon (IPyC) analysis of the last two AGR-5/6/7 coated particle batches (93172B and 93173B) and initiated documentation of the results in a data report.

- Analyzed precession electron diffraction (PED) data from Sites 4, 7, and 10 (in the silicon carbide [SiC] layer) from Particle AGR2-223-RS06. The grain boundary distributions in Sites 4 and 7 were statistically identical. The grain boundary distribution at Site 10 was different from the grain boundary distribution at either Site 4 or 7. The reason for this difference cannot be explained at this time.
- Completed transmission electron microscopy (TEM) imaging for estimating distribution, volume fraction, and number density of irradiation induced voids in multiple lamellae of Particles AGR1-632-034, AGR1-523-SP01, AGR1-131-066, AGR1-433-001, and AGR2-223-RS06.
- Completed characterization of irradiation-induced low-temperature alpha-SiC precipitates (within the bulk beta phase that predominates in the SiC layer) in Particles AGR1-632-034 and AGR2-223-RS06. Observed the intra-granular transport precipitation of palladium silicide at these alpha-SiC precipitates.
- Prepared manuscript for a journal article on the topic of intragranular palladium precipitates at the metamorphosed site of alpha-SiC.
- Received preliminary results from Los Alamos National Laboratory high-resolution TEM examination of Particle AGR1-532-SP01 UCO kernel.
- PhD candidate completed scanning TEM (STEM) and TEM training and is approved for independent work on UCO kernels at the Center for Advanced Energy Studies.
- INL hosted the Department of Energy (DOE) AGR TRISO Fuel Program review from July 18–19, 2017. INL and ORNL provided presentations on AGR program status and future work:

  INL presented:

  - AGR-2 post-irradiation examination (PIE) progress update (J. D. Stempien)
  - Status and plans for fuel reirradiation testing (P. A. Demkowicz)
  - Advanced microscopy and microanalysis (I. van Rooyen)
  - Effects of radiation damage on fission product transport (I. van Rooyen)
  - AGR-3/4 fission product mass balance (J. D. Stempien)
  - AGR-3/4 PIE destructive exams (J. D. Stempien)
  - AGR-5/6/7 fuel fabrication (D. Marshall)
  - AGR TRISO irradiation experiments (M. Davenport)
  - Air/moisture-ingress furnace development (J. D. Stempien)
  - AGR fuel program path forward (P. A. Demkowicz)
  - Nuclear Data Management and Analysis System (NDMAS) data management and archiving (N. Lybeck)

  ORNL presented:

  - AGR-2 PIE fuel compact destructive exams (J. D. Hunn)
  - AGR-2 safety testing (R. N. Morris)
  - Long-duration heating tests for silver release at intermediate temperatures (T. Gerczak)
  - High-temperature testing of surrogate materials in air and moisture (T. Gerczak)
  - Generation IV International Forum (GIF) leach-burn-leach (LBL) round-robin experiment (J. D. Hunn)

  - Fabrication of pyrolytic carbon (PyC)/SiC diffusion couples to study radiation enhanced diffusion in TRISO SiC (T. Gerczak).

- Nuclear Energy University Program project to measure silver transport in diffusion couples at the AGR TRISO fuels (R. Wahlen; University of Michigan with ORNL co-authors).

August

- Received the AGR-5/6/7 compact certification package from BWXT.
- Finalized a title transfer agreement between DOE and Kansas State University for the shipment of low-enriched uranyl nitrate crystals to the university.
- Completed x-ray computed tomography scanning on six compacts; three with 25% and three with 40% TRISO packing fractions. Data regression is still in progress.
- Submitted Level 2 milestone report, *Safety-Testing of AGR-2 UCO Compacts 6-4-2 and 2-3-1* (ORNL/TM-2017/439), which summarizes results from FY17 safety tests completed on two irradiated AGR-2 UCO fuel compacts in the ORNL CCCTF, with comparison of results to two previously completed 1600°C safety tests on similar AGR-2 compacts.
- Completed second FY17 shipment of AGR-2 irradiated compacts from INL to ORNL and submitted letter to document early Level 3 milestone completion.
- Completed burn-leach of graphite holder from the 1600°C safety test of AGR-2 UO_2 Compact 4-3-1.
- Initiated radiochemical analysis of CCCTF furnace internals for fission product release from 1800°C safety test of AGR-2 UCO Compact 2-3-2.
- Initiated 1600°C safety test of AGR-2 UO_2 Compact 4-2-1.
- Completed burn-leach of matrix from as-irradiated AGR-2 UCO Compact 2-2-1 and separated particles for IMGA survey.
- Completed post-burn-leach of particles deconsolidated from 1800°C safety-tested AGR-2 UCO Compact 2-3-2.
- Completed deconsolidation and pre-burn-leach of 1600°C safety-tested AGR-2 UO_2 Compact 4-3-1, and separated particles for IMGA survey.
- Completed measurement of key gamma-emitting fission product inventories in TRISO particles deconsolidated from 1700°C safety-tested UO_2 Compact 3-4-1 with the IMGA; multiple particles exhibited a reduced residual cesium inventory, as expected from the cesium release detected in the CCCTF.
- Initiated IMGA survey of particles deconsolidated from as-irradiated AGR-2 UCO Compact 2-2-1.
- Completed materialographic sample preparation and optical microscopy of selected particles from as-irradiated AGR-2 UCO Compact 6-2-3; analysis with scanning electron microscopy (SEM) and energy-dispersive spectroscopy is in progress.
- Completed SEM and EDS of particles from as-irradiated AGR-2 UCO Compact 5-4-2.
- Loaded six loose kernels (and two kernel fragments) from AGR-2 Compact 6-4-1 into separate graphite containers for reirradiation heating testing in the Neutron Radiography Reactor (NRAD) and the fuel accident condition simulator (FACS) furnace.
- Transferred loose kernels (and kernel fragments) from the Analytical Laboratory to the Hot Fuel Examination Facility (HFEF) for gamma counting prior to reirradiation heating tests.
- Completed radial deconsolidation of AGR-3/4 Compact 3-3.

- Completed precision gamma scanner tomographic scans on AGR-3/4 Capsule 10 outer ring.
- Completed physical sampling of AGR-3/4 inner and outer rings from Capsule 5.
- Completed physical sampling of AGR-3/4 inner and outer rings from Capsule 8.
- Counted select graphite samples from AGR-3/4 physical sampling on the HFEF out-of-cell gamma (HOG) station.
- Completed post-radial deconsolidation LBL (DLBL) of AGR-3/4 Compact 12-3.
- Completed LBL of all radial deconsolidation material from AGR-3/4 Compact 12-1.
- Began 1600°C heating test of AGR-3/4 Compact 3-2 in the FACS furnace.
- Began gamma counting of condensation plates from the AGR-3/4 Compact 3-2 heating test using the HOG station.
- Held 60% design review for the air/moisture ingress furnace.
- Completed shipment from INL to Pacific Northwest National Laboratory (PNNL) for analysis of graphite samples generated from physical sampling of inner and outer rings from AGR-3/4 Capsules 3 and 7.
- Collected STEM, EDS, and PED data on Lamellae 7, 8, and 9 (Area B) of Particle AGR2-223-RS036.
- Completed report section on PED of Lamellae 4, 5, and 6 (Area A) of Particle AGR2-223-RS06.
- Received kernel examination report from Los Alamos National Laboratory on Particle AGR1-532-SP01.
- Completed kernel data collection on Particle AGR1-433-001.
- Submitted journal article “A novel nucleation pathway in crystalline solids under neutron irradiation” (S. Meher, I. J. van Rooyen, and T. M. Lillo).
- Issued report, *Acceptance Test Data for BWXT Coated Particle Batches 93172B and 93173B* (ORNL/TM-2017/039).
- Completed shipment from BWXT to ORNL of AGR-5/6/7 fuel compacts and overcoated particles for confirmatory LBL analysis.
- The journal article “Impact of gap size uncertainty on calculated temperature uncertainty for the advanced gas reactor experiments” (Binh Pham, Jeff Einerson, Grant Hawkes, Nancy Lybeck, and Dave Petti) was accepted for publication in Nuclear Engineering and Design.

September

- Received an updated draft plan from BWXT for the disposition of government-furnished equipment for AGR fuel fabrication and the associated uranium-bearing materials. The plan will be used as a basis for defining disposition work scope.
- Shipped AGR fuel compacts and TRISO fuel particles overcoated with resinated graphite matrix powder from BWXT to ORNL for confirmatory analysis of the uncontained uranium defect fractions. The data will be available in early Calendar Year 2018.
- Completed 1600°C safety test of AGR-2 South African UO_2 Compact 4-2-1.
- Completed demonstration of furnace for irradiated TRISO-particle testing operation for radiological control technicians and Irradiated Fuels Examination Laboratory hot cell staff to obtain approval for furnace operation with irradiated particles.

- Completed post-burn-leach (final step of DLBL) of 1700°C safety-tested AGR-2 UO_2 Compact 3-4-1; analysis of leachates is in progress.
- Completed deconsolidation and pre-burn-leach of as-irradiated AGR-2 UCO Compacts 6-2-3 and 2-2-1.
- Completed survey of cesium and cerium retention in TRISO particles deconsolidated from as-irradiated AGR-2 UCO Compact 2-2-1 with the IMGA; no particles exhibited preferential cesium loss indicative of failed SiC, one particle had equally low inventories of both cesium and cerium, which has been observed previously in particles with unusually low initial fissile inventory.
- Completed x-ray tomography of particles from 1800°C safety-tested AGR-2 UCO Compact 2-3-2; one particle identified with the IMGA as having preferential cesium loss had an obvious SiC degradation site.
- Completed x-ray tomography, materialographic sample preparation, and optical microscopy on randomly selected particles from 1600°C safety-tested AGR-2 UCO Compact 6-4-2.
- Completed analysis with SEM and EDS of particles from as-irradiated AGR-2 UCO Compacts 6-4-2 and 2-3-2.
- Completed fabrication of graphite mounts for impact cracking and reirradiation of AGR-2 particles and completed preparation of fixtures for particle loading, impact cracking, and x-ray tomography; final tests are in progress prior to preparation of irradiated particle specimens.
- Received approval from China to ship ORNL-fabricated round-robin experiment samples containing TRISO particles with simulated LBL defects mixed with surrogate TRISO particles and a graphite impurity standard as part of an LBL quality control benchmarking collaboration through the GIF.
- Completed 30% of the planned test matrix for high-temperature stream oxidation of graphitic matrix material; fabricated 200 additional green compacts for graphitic matrix steam oxidation kinetics evaluation.
- Located niobium flux wire from AGR-2 Capsule 2 graphite holder, and initiated burn of that holder.
- Transferred loose kernels from AGR-2 Compact 6-4-1 to HFEF for reirradiation heating tests.
- Completed pre-reirradiation gamma counting, 4-day reirradiation in NRAD, and post-reirradiation gamma counting of AGR-2 Compact 6-4-1, Kernels 11, 17, 19, and 39.
- Ran heating test with the four reirradiated AGR-2 Compact 6-4-1 kernels (numbers 11, 17, 19, and 39) in the FACS furnace for about 10 hours at 1600°C before increasing chamber pressure forced test termination. The inlet to the fission gas monitoring system cold trap became plugged. Test was restarted and ran for several hours before the fission gas monitoring system gas line re-plugged. The problem was traced back to ice formation from moisture trapped on a charcoal filter used to capture iodine.
- Completed heating test of AGR-3/4 Compact 3-2 (330 hours at 1600°C, 48 hours at 1700°C) in the FACS furnace.
- Counted all condensation plates from the AGR-3/4 Compact 3-2 heating test on the HOG station.
- Completed HOG counting of graphite samples from AGR-3/4 Capsule 5 and 8 inner and outer rings prior to shipment to PNNL.
- Completed shipment of samples from AGR-3/4 Capsule 5 and 8 inner and outer rings to PNNL.
- Completed post-burn-leach of AGR-3/4 Sink 11, and recovered the missing iron fluence wire from Sink 11.

- Completed repeat gamma counts of AGR-3/4 Capsule Foils 1, 3, 7, and 8.
- Completed repeat gamma counts of AGR-3/4 Capsule 3 and 8 spacers. Repeat counts will be used to judge repeatability and proper counting geometry.
- Completed burn-leach of the four radial segments of AGR-3/4 Compact 3-3. Axial deconsolidation and burn-leach is in progress.
- Issued “Radial Deconsolidation and Leach-Burn-Leach of AGR-3/4 Compacts 3-3, 12-1, and 12-3”, INL/EXT-17-43182documenting completion of radial deconsolidation and LBL of the radial material from two irradiated AGR-3/4 compacts. This report fulfills a Level 3 milestone (M3AT-17IN15010410). This report also discusses a third compact that completed radial deconsolidation but for which LBL steps are in progress.
- Completed pressure testing of the benchtop air-moisture ingress furnace.
- Completed 60% design review, comment collection, and comment resolution to fulfill a Level 2 milestone (M2AT-17IN15010412) for the air/moisture ingress furnace.
- Initiated experiment safety analysis for a full compact reirradiation in NRAD and updated the experiment safety analysis (for individual particles or kernels) to allow titanium reirradiation capsule in addition to the existing aluminum reirradiation capsule. Simulations indicate that thermal flux in the titanium capsule is 14% less than in the aluminum capsule. However, particle samples can be accessed immediately following reirradiation, instead of waiting approximately 1 day (12.5% of the I-131 half-life).
- Received Nuclear Science User Facilities rapid turnaround experiment funds with University of Florida. Project principle investigators: Yong Yang, Isabella van Rooyen, Mukesh Bachhav; graduate student team member: Matthew Cook. Experiment title: Characterize the Irradiated Microstructure and Understand the Fission Product Behavior in an Irradiated AGR-1 TRISO Fuel Particle Kernel.
- Initiated LBL analysis of AGR-5/6/7 overcoated particles to evaluate if the overcoating process introduced particle defects.

1.2 High-Temperature Materials Development

Highlights of high-temperature materials development activities during July through September 2017 are as follows:

July

- Completed interrupted creep test of large-radius U-notch welded Alloy 617 specimen (800°C, 80 MPa, interrupted at 800 hours).
- Performed metallographic analysis of interrupted weld metal test. The large-radius U-notch was contained entirely within the weld metal, as desired. No creep damage was observed in the cross section of the notch.
- Continuing four creep notch tests (large radius U-notch test at 750°C, 145 MPa, and small-radius U-notch tests at 750°C, 145 MPa; 800°C, 80 MPa; and 900°C, 36 MPa.
- Sections of the High Temperature Alloy 617 Section III Division 5 Code Case relating to design fatigue curves, physical properties, and time-dependent allowable stresses are currently under recirculation balloting after minor editorial corrections.

August

- INL staff participated in the American Society of Mechanical Engineers (ASME) Code Week in Minneapolis, MN.

- Sections of the Alloy 617 ASME Code Case for time-dependent allowable stresses and physical properties passed ASME Section III Subgroup on High Temperature Reactors and Subgroup on Materials, Fabrication and Evaluation and will go to ASME Section II subgroups for ballot.
- Alloy 617 fatigue design curves were passed by voice vote by ASME Section III Working Group Creep-Fatigue and Negligible Creep and Working Group Fatigue Strength and will next go to ASME Section III Subgroup on Elevated Temperature Design for ballot.
- Finished creep rupture tests of base metal, large-radius U-notch at 750°C, 145 MPa, as well as two base metal, small-radius U-notch tests at 900°C, 36 MPa and 800°C, 80 MPa. Two tests have been started, large- and small-radius base metal U-notch specimens, both at 1000°C, 20 MPa.
- Completed "Overview of Alloy 617 Notched Specimen Testing", INL/EXT-17-43070, August 2017, for Level 3 milestone M3AT-17IN1601042.

September

- Creep rupture tests are ongoing: small-radius U-notch test at 750°C, 145 MPa, as well as small- and large-radius U-notch tests at 1000°C, 20 MPa.
- Performed metallographic analysis of specimens previously tested to rupture at 800°C, 80 MPa (small- and large-radius U-notch specimens) and 750°C, 145 MPa (large-radius U-notch specimens).
- Continued microstructural analysis on interrupted notched creep test on Alloy 617 weldment.
- Completed Level 2 milestone entitled "Complete Update to High Temperature Alloy 617 Code Case to Reflect Ballot Comments."
- Moved High Temperature Code Case sections on design stress allowables and physical properties to ballot at the ASME Section III Subgroup on Materials, Fabrication and Evaluation and ASME Section II Subgroup on Non-Ferrous Alloys.

1.3 Graphite Development and Qualification

Highlights of graphite development and qualification activities during July through September 2017 are as follows:

July

- Measured gas diffusivity on 30 graphite samples (spanning six grades) to further the development of a comprehensive graphite oxidation model applicable to all nuclear graphite grades.
- Completed initial thermal creep studies on four different nuclear graphite grades; NBG-18, 2114, IG-110, and PCEA. The changes to the pore microstructure will be analyzed and compared to irradiated creep specimens to elucidate the effect of microstructure evolution on irradiation material property behavior.
- Received thermal creep specimens for three nuclear graphite grades (Gilsocarbon, IG-110, and NBG-18) from Manchester University. As part of this international collaboration, INL has agreed to strain these specimens in the graphite thermal creep furnace to induce thermal strains and investigate thermal and irradiation creep mechanisms in nuclear graphite.
- Issued letter report, "Current progress in determining oxidation results of graphite grade 2114," by July 10, 2017 (5 days ahead of schedule).
- Issued report, *HTV Post Irradiation Examination (PIE) Results and Analysis* (ORNL/TM-2017/292), in accordance with the Advanced Reactor Technologies (ART) Graphite FY17 memorandum purchase order.

- Completed Level 3 milestone M3AT-17IN1603038, “Validate and Fully Release the Data from Five Different Billets of Candidate Nuclear Graphite Grades to the Nuclear Data Management and Analysis System (NDMAS) After Completing All Remaining Physical and Mechanical Property Measurements.”
- Completed Level 3 milestone M3AT-17IN1603039, “Complete GIF PMB High Level Deliverable (HLD) in Graphite Fracture (Task 1.3) as Designated in the GIF VHTR Materials Project Plan (GIF VMPP),” by July 30, 2017.

August

- Submitted journal article “Beyond the classical kinetic model for chronic graphite oxidation by moisture in high temperature gas-cooled reactors” (C. Contescu, R. Mee, Y. Lee, J. Arregui-Mena, C. Gallego, T. Burchell, J. Kane, and W. Windes) to Carbon journal.
- Delivered material property test data, compiled in five different engineering calculations and analysis reports, to the NDMAS database following completion of unirradiated material property testing on five different graphite billets within the baseline activity, a Level 3 milestone (M3AT-17IN1603038).
- Passed the subgroup ballot for ASME Boiler and Pressure Vessel Code for composites (HHB) (except Article HHB 3000: Design, which is hoped to be approved on recirculation ballot). The consolidated HHC code will be bought forward for Section III approval soon. Additional nonmandatory appendixes will be prepared next FY (if adequately funded).
- Commenced evaluation of prospective locations for thermogravimetric analyzer oxidation of irradiated graphite specimens.
- Completed the experimental portion of a scoping study to investigate graphite strength under various oxidizing conditions. The engineering failure strength of graphite has been measured for three oxidizing conditions (low, medium, and high temperature) after total mass loss conditions corresponding nominally to 5 and 10%. These results suggest (1) oxidation can significantly lower strength; (2) the oxidizing conditions influence the observed strength; and (3) due to microstructural differences, strength does not follow the same trend for each grade.
- Began code modification to the graphite oxidation model, adding slight changes to the mass transport physics to better fit a wide variety of graphite grades. Upon completion, simulation results will be compared directly to experimental results over a range of temperatures for multiple graphite grades to demonstrate the flexibility and universal applicability of the model. Additional experiments are needed to measure key microstructural inputs.
- Completed Level 3 milestone M3AT-17IN16030310, “Complete International Atomic Energy Agency (IAEA) Technical Document Discussion of Nuclear Grade Graphite Oxidation in Modular High Temperature Gas-Cooled Reactors.”

September

- Inserted AGC-4 into the Advanced Test Reactor (ATR) east flux trap to continue its irradiation campaign, which was interrupted by Ki-Jang Research Reactor.
- Completed Level 2 milestone M2AT-17IN1603025, “Assembly of the AGC-5 Upper Cylinder Housing.”
- Hosted and participated in the International Nuclear Graphite Specialists Meeting (INGSM) in Baltimore, MD, September 17–22, 2017.
- Submitted journal article “Beyond the classical kinetic model for chronic graphite oxidation by moisture in high temperature gas-cooled rectors” (C. Contescu, R. Mee, Y. Lee, J. Arregui-Mena, C. Gallego, T. Burchell, J. Kane and W. Windes); currently under review at Carbon journal.

1.4 Methods

Highlights of methods activities during July through September 2017 are as follows:

July

- Issued the test acceptance report for the first Oregon State University (OSU) High Temperature Test Facility (HTTF) matrix test, PG-22.
- OSU completed removal of the HTTF core blocks and heater rod components; the latter were reassembled outside of the reactor for examination.
- Submitted a Level 3 milestone report, *IAEA CRP on HTGR UAM: Specifications for Phase II Exercise 1 (Depletion) and Nominal Results* (INL/LTD-17-41017), on the specifications for the Exercise II-1 depletion cases of the International Atomic Energy Agency (IAEA) Coordinated Research Project (CRP) on high-temperature gas-cooled reactor (HTGR) uncertainties. This report details the preliminary INL results obtained with the Standardized Computer Analyses for Licensing Evaluation (SCALE)/SAMPLER code and proposes a set of output parameters to be compared before the next research coordination meeting that will be held in May 2018 in Vienna, Austria.
- Initialized the post-processing of participants' data for the comparison report on Phase I of the CRP that is due August 30, 2017. This report will include the results submitted for all the lattice exercises, as well as the stand-alone thermal hydraulic and Very High Temperature Reactor Critical (VHTRC) experimental validation cases.

August

- Completed RELAP5-3D assessment calculations using data from OSU HTTF Test PG-22.
- Submitted a Level 3 milestone report, *IAEA Coordinated Research Project on HTGR Uncertainties in Modeling: Comparison of Phase I Nominal, Uncertainty, and Sensitivity Results* (INL/LTD-16-40699), on the comparison results obtained for the Phase I exercises of the IAEA CRP on HTGR uncertainties. This report details the results submitted for all of the cell, single block, and supercell lattice exercises, as well as the stand-alone thermal hydraulic and VHTRC experimental validation cases.

September

- Completed a Level 3 milestone report, *RELAP5-3D Assessment Using High Temperature Test Facility Test PG-22* (INL/EXT-17-43120), on September 8, 2017, one week ahead of schedule.
- OSU developed a new HTTF heater rod design and cost estimates for replacing damaged facility equipment.
- Continued with the specification of the Phase II exercises for the IAEA CRP on HTGR uncertainties. The full-core neutronics and thermal fluids cases will be tested using the INL codes PHISICS/RELAP5-3D and the ORNL code suite SCALE/SAMPLER before the specification document is released to the CRP group for review in March 2018.
- Initialized the comparison of the Phase III lattice cases for the Organization for Economic Cooperation and Development (OECD)/Nuclear Energy Agency (NEA) Modular HTGR (MHTGR)-350 Benchmark. Two reports on Phases I and III will be released to the OECD for review by early January 2018 and will detail the results submitted by participants from six intuitions in South Korea, Germany, and the United States.

2. SIGNIFICANT ACCOMPLISHMENTS

2.1 Fuels Development

2.1.1 Fuel Development and Fabrication

2.1.1.1 AGR Fuel Compact Certification Package. The fuel certification package and Quality Control Deficiency Notices were received from BWXT. The Quality Control Deficiency Notices document instances where the fuel did not conform to the AGR-5/6/7 fuel specifications for outer pyrolytic carbon (OPyC) thickness and uncontained uranium defect fractions. ECAR-3873 documents the reasoning as to why the nonconforming fuel was acceptable for use. The arguments are:

- The OPyC layer is adequate for its intended function especially since the thickness distribution is very narrow, so that extremely thin OPyC layers are very unlikely
- Uncontained uranium defect fraction specifications are written to the needs of a high-temperature reactor and not specifically tuned for the irradiation experiments
- The uncontained uranium will result in a higher than desired background of fission product releases during irradiation, but it is not expected to be so high as to prevent collection of meaningful and useful data.
- Refabricating fuel without an understanding of why the fuel did not meet specifications had little probability of producing fuel that would conform to the specifications and the time lost in refabrication and characterization would jeopardize access to the essential flux trap in ATR.

References

ECAR-3873, "Acceptance of Nonconforming Fuel for the AGR-5/6/7 Irradiation Experiments," Rev. 0, Idaho National Laboratory, September 2017.

2.1.1.2 Transfer of Low-Enriched Uranyl Nitrate Crystals to Kansas State University. A title transfer agreement was finalized between DOE and Kansas State University to enable transferring a few grams of uranyl nitrate crystals, enriched slightly under 20% U-235, for use in developing fission monitoring probes. Once the title transfer was completed, the crystals were shipped to and received by Kansas State University.

2.1.1.3 Defective IPyC Fraction and Pyrocarbon Anisotropy of Coated Particle Batches 93172B and 93173B. Coated particle batches J52O-16-93172B and J52O-16-93173B were produced by BWXT as part of the production campaign for the AGR Reactor Fuel Development and Qualification Program's AGR-5/6/7 irradiation test in the INL ATR, but were not used in the final fuel composite. However, these batches may be used as demonstration production-scale coated particle fuel for other experiments. Each batch was coated in a 150-mm-diameter production-scale fluidized-bed chemical vapor deposition furnace. The TRISO-coated particle batches were sieved twice to upgrade the particles by removing oversized and undersized material, and the upgraded batches were designated by appending the letter B to the end of the batch number. Two samples each were riffled from upgraded TRISO batches 93172B and 93173B and shipped from BWXT to ORNL for determination of the PyC anisotropy and defective IPyC fraction. Detailed results have been documented in Helmreich et al. 2017.

Table 1 summarizes the PyC anisotropy results. Both analyzed batches satisfied the AGR-5/6/7 fuel specification for PyC anisotropy, with average diattenuation (N) values below the specified upper limits of $N \leq 0.0170$ for the IPyC layer and $N \leq 0.0122$ for the OPyC layer. The higher allowable IPyC diattenuation is related to the fact that pyrocarbon anisotropy is measured after all TRISO coatings are deposited. During SiC deposition, the IPyC layer is heated to approximately 1550°C for over 2 hours; this heat treatment after IPyC deposition at lower temperatures increases the average anisotropy of the layer (Hunn et al. 2007). Further increase in the average anisotropy can be expected when compacts are heat treated to even higher temperatures. For example, after heating particles to 1800°C to simulate compacting as described above, the average anisotropy of both the IPyC and OPyC layers increased, as shown in Table 1.

Table 1. Summary of pyrocarbon anisotropy for coated particle batches 93172B and 93173B.

Coating Batch	Average Anisotropy As-Deposited TRISO[a]			After Heating to 1800°C
	IPyC	OPyC	IPyC	OPyC
93172B	N=0.0154 OPTAF=1.0313	N=0.0099 OPTAF=1.0199	N=0.0177 OPTAF=1.0361	N=0.0138 OPTAF=1.0279
93173B	N=0.0139 OPTAF=1.0282	N=0.0098 OPTAF=1.0198	N=0.0174 OPTAF=1.0353	N=0.0136 OPTAF=1.0276

[a] As-deposited anisotropy is used for comparison to fuel specification limits.

The upper limit on the defective IPyC fraction is specified as $\leq 10^{-4}$ with a requirement that statistical sampling demonstrate with at least 95% confidence that the batch has a defect fraction less than this limit. Acceptance testing was performed by riffling two random subsamples from each batch with the appropriate number of particles to apply two predetermined acceptance criteria derived using binomial distribution statistics. The Stage 1 acceptance criteria was two or less defects in a random group of at least 62,956 particles. The Stage 2 acceptance criteria was six or less defects in a random group of at least 118,422 particles. The analysis results from the first riffled subsample were used for Stage 1, and the combined results from both subsamples were used for Stage 2. Target weights for the riffled subsamples were determined based on the average particle weight, with a sufficient margin based on the uncertainty in the average particle weight to ensure the subsamples provided at least the required minimum number of particles, while minimizing overshoot. Minimizing overshoot is important because the probability that a sublot with an acceptable defect population will satisfy the acceptance criteria decreases as a function of increasing difference between the actual number of particles analyzed and the minimum required. The exact number of particles in each subsample was determined by counting the particles in the x-ray radiographs acquired for the defective IPyC analysis. As shown in Table 2, both coating batches passed the Stage 2 criteria. Both coating batches also passed the Stage 1 criteria, but combined results are presented in Table 2 because of the higher statistical accuracy of the larger sample size.

Table 2. Summary of defective IPyC for coated particle batches 93172B and 93173B.

Coating Batch	Number of Particles in Analyzed Sample	Number of Particles with Defective IPyC	Measured Defect Fraction in Sample	Maximum Defect Fraction at 95% Confidence
93172B	120,048	3 (pass)	2.50×10^{-5}	6.46×10^{-5}
93173B	120,897	1 (pass)	8.27×10^{-6}	3.93×10^{-5}

References

Helmreich, G. W., J. D. Hunn, D. J. Skitt, J. A. Dyer, and A. Schumcher, 2017, *Acceptance Test Data for BWXT Coated Particle Batches 93172B and 93173B*, ORNL/TM-2017/039, Oak Ridge National Laboratory, May 2017.

Hunn, J.D., G.E. Jellison Jr., and R.A. Lowden. 2007. "Increase in pyrolytic carbon optical anisotropy and density during processing of coated particle fuel due to heat treatment." J. Nucl. Mater. 374: 445-452.   Safety Testing and Post-Irradiation Examination

2.1.1.4 AGR-3/4 Completion of Three Compact Radial Deconsolidations and Two LBLs

Introduction

The following are excerpts from Stempien 2017. This report was submitted on September 8, 2017, in fulfillment of Level 3 milestone M3AT-17IN15010410.

The AGR-3/4 experiment was designed to investigate the transport of fission products in fuel compacts, nuclear graphite, and graphitic matrix material. Measurements of radial fission product concentration profiles within a compact outside of the fuel particle SiC layers cannot be accomplished with the axial deconsolidation technique used previously. Radial deconsolidation sequentially removes radial segments of compacts so that each segment can be analyzed separately for fission products and a fission product concentration profile can be constructed. Radial deconsolidation was completed on irradiated AGR-3/4 Compacts 3-3, 12-1, and 12-3, and LBL was completed on the radial segments collected from Compacts 12-1 and 12-3.

One of several features of AGR-3/4 that set it apart from AGR-1 and AGR-2 is the incorporation of 20 designed-to-fail (DTF) particles in each compact in addition to the approximately 1872 TRISO-coated "driver" fuel particles. Fuel kernels in DTF particles were coated only with a thin (20-µm thick) pyrocarbon layer. This layer was intentionally fabricated with a high anisotropy, such that it would be likely to fail during the irradiation (Collin 2015b), resulting in up to 20 exposed fuel kernels per compact. Driver particle fuel kernels were fully TRISO-coated with the buffer layer, IPyC, SiC, and OPyC layer. To reiterate, each AGR-3/4 compact contains approximately 1872 driver fuel particles and precisely 20 DTF particles.

All AGR-3/4 fuel particles (both driver particles and DTF particles) contain low-enriched UCO (a uranium carbide, uranium oxide mixture) fuel kernels approximately 350 µm in diameter manufactured at BWXT Nuclear Operations Group (Lynchburg, VA). The U-235 enrichment was 19.7%. As shown at right in Figure 1, the DTF particles (highlighted in red) were aligned in each compact roughly along the compact radial centerline. The white circles in Figure 1 are the driver particles. The DTF particles were fabricated at ORNL by applying a single 20-µm-thick PyC coating to the kernels produced at BWXT. Driver fuel particles were fabricated at ORNL by applying TRISO coatings to the kernels.

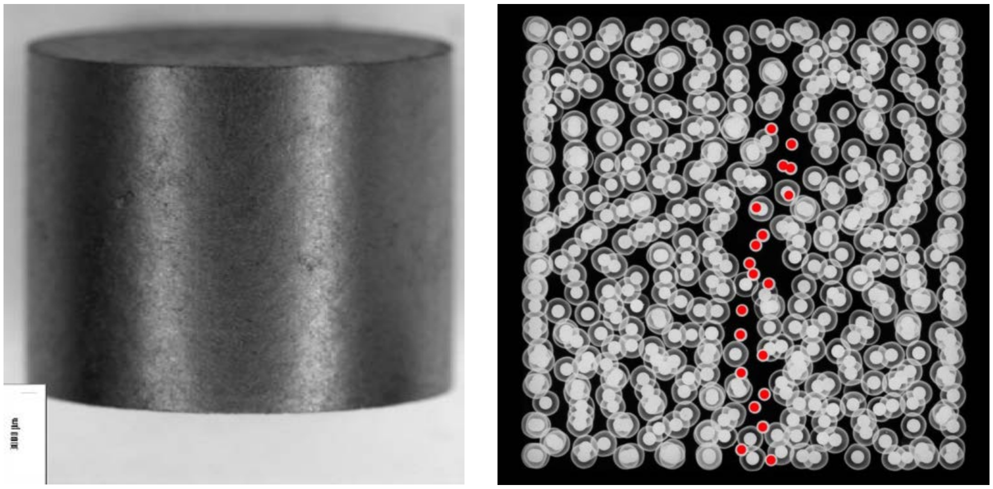

Figure 1. Image of an AGR-3/4 fuel compact (left) and x-ray side view image (right) (Hunn, Trammell, and Montgomery 2011). DTF particles are highlighted with red dots in the x-ray image.

Figure 2 plots the time-averaged, volume-averaged (TAVA) irradiation temperature and fast fluence for each of the four compacts in each of the 12 AGR-3/4 capsules. Moving from left to right on the x-axis, compacts are plotted in order from the bottom of the test train to the top. The sine-shape of the axial fluence profile is clearly visible, but the axial variation in the TAVA temperature is flatter. The fast fluences and TAVA irradiation temperatures for Compacts 3-3, 12-1, and 12-3 are highlighted in Figure 2. In each compact, the UCO fuel kernel lot is G37V-20-69303, the TRISO-coated driver fuel particle lot is LEU03-09T (renamed as LEU03-10T), and the DTF particle lot is LEU03-07DTF. Estimates of the number of failed DTF particles in each AGR-3/4 irradiation capsule are discussed in (Collin 2015a) and (Scates 2015). For Capsule 3, it appears that all 20 DTF particles failed in each of the four compacts. Thus, 20 failed DTF particles are expected to be present in Compact 3-3. On average, between 10 and 13 DTF particle failures should be expected in each Capsule 12 compact.

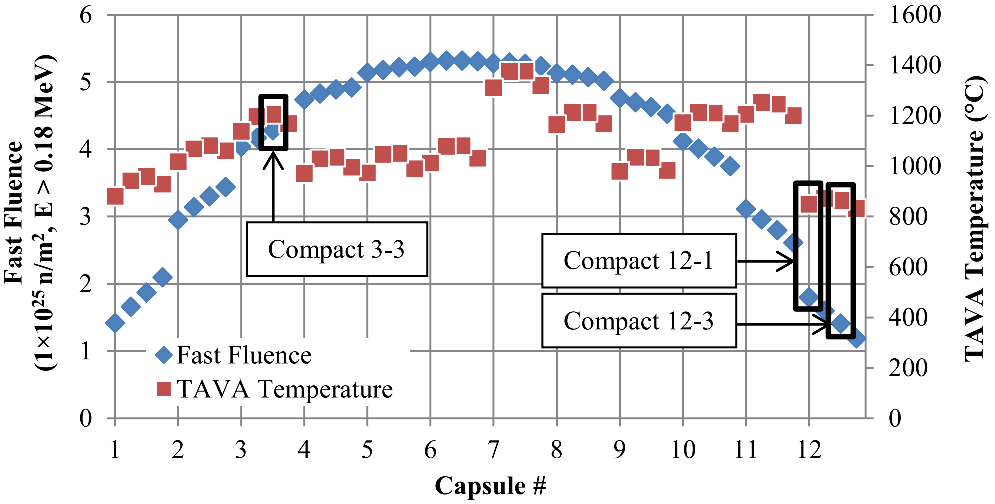

Figure 2. Calculated fast fluence and TAVA temperature for each of the four compacts in each of the 12 AGR-3/4 capsules. Fluences and temperatures from Hawkes 2016 and Sterbentz 2015, respectively.

Radial Deconsolidation Methodology

The AGR-3/4 experiment was designed to investigate the transport of fission products in fuel compacts, nuclear graphite, and graphitic matrix material. Measurements of fission product concentration profiles (axially and radially) within AGR-3/4 samples (primarily graphite rings and compacts) are significant analyses in the AGR-3/4 PIE plan (Demkowicz 2017). Deconsolidation and subsequent LBL are used to measure fission products within the fuel compact outside of the fuel particle SiC layers. Compact deconsolidation is the electrolytic oxidation of the compact graphitic matrix. Oxidation of the compact breaks up the compact matrix, TRISO particles are liberated, and TRISO particles and remnants/debris from the matrix are collected on a porous, fused silica frit (also referred to as a thimble) at the bottom of the deconsolidation apparatus. There are two methods of compact deconsolidation, “axial” and “radial”. In “axial” deconsolidation, the compact matrix is disintegrated from the bottom to the top in a single step. In “radial” deconsolidation, the compact is rotated against a screen and material is removed from the outside in. Radial deconsolidation has three important benefits that traditional axial deconsolidation does not. First, and most importantly, radial deconsolidation enables measurements of the radial fission product profile within a compact outside of the TRISO SiC layer. Second, radial deconsolidation allows collection and analysis of particles from specific radial regions of a compact. In-pile radial temperature gradients in compacts may result in differences in fuel performance between particles from different radial zones of a compact. Third, radial deconsolidation allows radial segments of the compact to be removed without disturbing the DTF particles located approximately in the center of the compact. If failed DTF particles were deconsolidated along with other portions of the compact, the DTF fuel kernels would dissolve in the acid solution and make measurements of the fission product content in the compact matrix impossible because the DTF kernels would overwhelm the contribution from fission products retained in the matrix.

Significant process development for the radial deconsolidation method was performed at ORNL (Helmreich, Montgomery, and Hunn 2015) and at INL. Parameters investigated by Helmreich, Montgomery, and Hunn 2015 included nitric acid concentration, speed of compact rotation, contact force between the compact and a platinum-rhodium screen serving as the anode, and the current applied to the compact. Development work at INL focused on designing a radial deconsolidation apparatus to function in a hot cell that could be operated with master-slave manipulators. Figure 3 shows the radial deconsolidation apparatus developed at INL that was installed in Cell 5 at the Analytical Laboratory. One end of the compact is glued to one end of a 6-mm-diameter hollow stainless-steel shaft (referred to from hereon as a "rod") using AA-CARB 61 conductive epoxy from Atom Adhesives. On the other end of the rod is a gear that is driven at 10 rpm by a direct current (DC) electric gearmotor. A platinum wire is also glued into the rod such that it protrudes from the compact-epoxy interface. This wire facilitates electrical contact for axial deconsolidation of the compact core that remains after radial deconsolidation. With the compact and the stainless-steel deconsolidation rod in place, the micrometer is used to lower the height of the rod and compact so that the rod is just within the mouth of the beaker (Figure 4). Figure 4 shows that the platinum-rhodium screen anode behind the compact is fixed to a high-density polyethylene paddle, and the screen/paddle is adjusted by insertion of a high-density polyethylene wedge behind the paddle so that the screen makes consistent, even contact with the compact.

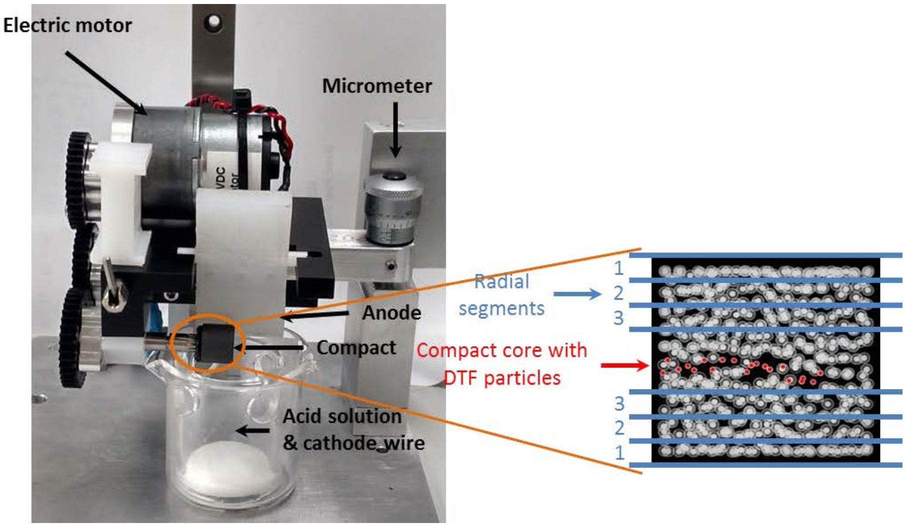

Figure 3. Radial deconsolidation apparatus and depiction of compact (x-ray image) indicating three radial segments and a central core with the DTF particles.

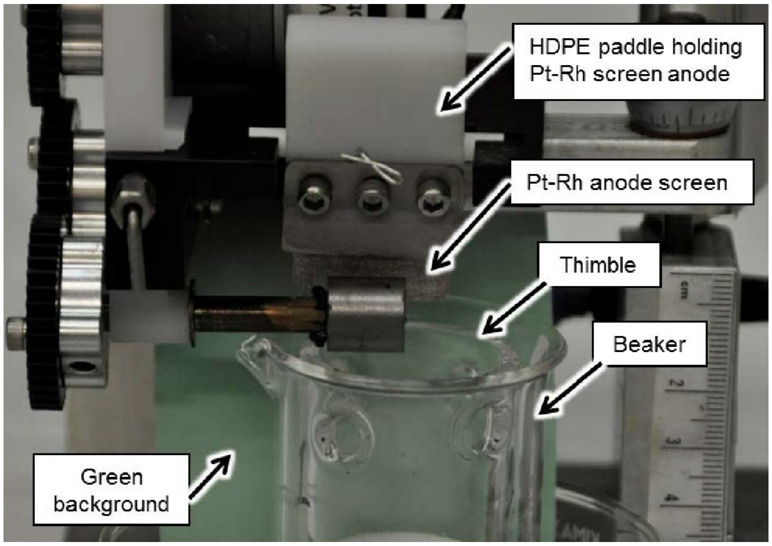

Figure 4. Unirradiated AGR-3/4 compact mounted to deconsolidation rod with platinum-rhodium anode in place behind the compact. Green screen behind the deconsolidation rod aids image analysis.

The electrical leads to the platinum-rhodium anode screen and the cathode wire (inserted in the space between the walls of the thimble and the beaker) are connected to a DC power supply. Then, the compact rotation is started, and the top of the compact is rotated toward the platinum-rhodium anode screen. With the anode and cathode leads connected, the compact in contact with the anode, and the compact rotating, 8M nitric acid is added to the beaker (which also fills the thimble due to the porous frit in the bottom of the thimble and the holes toward the top of the thimble). Acid is added until it just contacts the compact. With a complete electrical circuit between the anode, cathode, compact, and nitric acid, contact between the compact and the anode screen helps to remove deconsolidated matrix material allowing particles to come loose and fall to the bottom of the thimble. The DC power supply was operated in current control mode (constant voltage mode) and the voltage was adjusted manually such that the electrical power applied to the compact during deconsolidation is just less than 10 W.

With the compact rotating, radial deconsolidation proceeds for a period of time (typically 15 to 20 minutes to remove approximately 0.5 to 1 mm of the compact diameter), and then the deconsolidation solution is changed and a new thimble is put in place. A measurement of compact diameter is made using optical techniques at the conclusion of each radial deconsolidation step. Each deconsolidation solution, and the particles and matrix debris collected in each thimble, are stored in separate, labeled containers. Up to four 15- to 20-minute segments of radial deconsolidation are used. After three to four segments, enough compact material has been removed that the epoxy holding the compact to the rod (and/or the deconsolidation rod itself) begins to come in contact with the anode screen and the compact itself no longer has uniform contact with the anode screen. At this point, the radial portion of the deconsolidation is halted. The deconsolidation solution produced from each radial segment is analyzed for gamma-emitting fission products and undergoes analysis for beta-emitting Sr-90. LBL of the thimble material from each radial segment is performed, and a random sample of 30 driver fuel particles from each thimble is selected for particle gamma surveys. A traditional axial deconsolidation is then performed on the remaining compact core.

Image Analysis Methodology

For radial deconsolidation to give fission product concentrations within radial segments of a compact, the diameter of the compact must be known at the beginning of radial deconsolidation and at the end of each segment of radial deconsolidation. The development work performed at ORNL produced a program called “FrameGrabber” (written in MATLAB) for measuring the diameter of a compact by analyzing video captured while the compact rotated (Helmreich, Montgomery, and Hunn 2015). Videos of the as-irradiated compact were captured before beginning radial deconsolidation. This allowed a comparison of the diameter measured from the image analysis to the compact diameter measured from post-irradiation metrology.

After importing the video into FrameGrabber, the user receives a series of prompts. The first prompt asks for the diameter of the deconsolidation rod (6 mm). The rod serves as a standard that the compact is measured against. The second prompt asks if the user wants the program to rotate the image so that the rod and compact are horizontally level. The third prompt asks for the number of frames per compact rotation. The fourth prompt asks how many of the frames should be analyzed per compact rotation. Then, a prompt asks the user to draw a bounding box around the deconsolidation rod and a separate box around the compact. FrameGrabber will then work within these boxes to define the upper and lower edges of the rod and compact. For each frame analyzed, FrameGrabber generates an image of that frame with overlays of the boundaries of the compact that it has determined and projections of the upper and lower edges and center of the deconsolidation rod. An example of a frame with these overlays is given in Figure 5 for Frame 146 from analysis “11k_2_DSC_4739” from Compact 3-3.

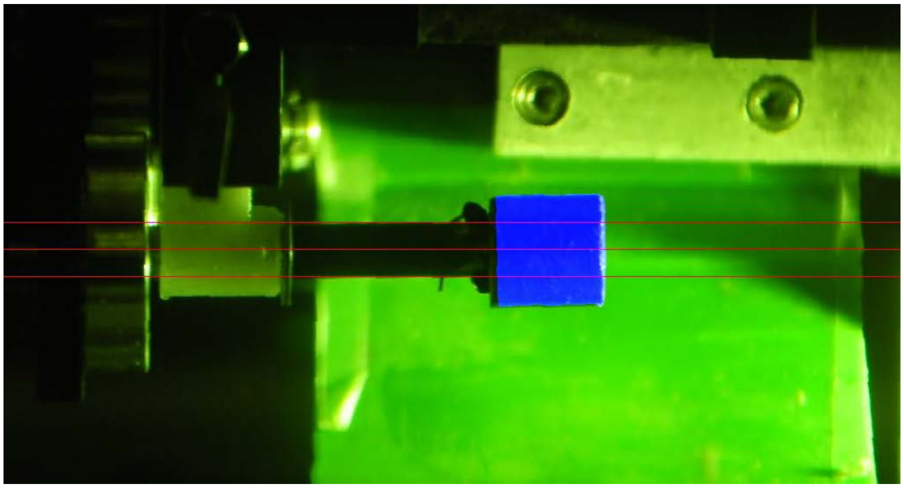

Figure 5. Blue shading shows the compact region determined by FrameGrabber for Compact 3-3. (Frame 146 from analysis 11k_2_DSC_4739.) Red lines denote deconsolidation rod center and upper and lower edges.

Dimensional Measurements Summary

Compact 3-3 had an as-irradiated diameter of 12.124 mm, ±0.0058 mm (Stempien et al. 2016). Generally, radial deconsolidation is continued until contact with the rod or epoxy holding the compact to the rod prevents further compact deconsolidation. After the third segment of radial deconsolidation, there appeared to be sufficient compact material remaining to warrant a fourth segment of radial deconsolidation. A fourth period of radial deconsolidation was run for 15 minutes at approximately 10 W. At the 15-minute mark, the compact fell off the rod, the deconsolidation was halted, and the diameter of the compact was measured by contact measurements using analog calipers. Two caliper measurements were taken at each of three locations along the length of the compact. Table 5 summarizes the change in compact diameter and volume after each of the four segments of radial deconsolidation. LBL of the thimbles collected from radial deconsolidation is currently in progress. Axial deconsolidation of the compact core has been performed, and LBL of the axial deconsolidation material will follow LBL of the radial material. Gamma surveys of driver fuel particles will begin as particles become available.

Table 3. Summary of Compact 3-3 diameter change, new diameter after each segment of deconsolidation, and the volume of the compact material removed.

Parameter	Segment 1	Segment 2	Segment 3	Segment 4
Radial deconsolidation time (min)	15	15	16	15
Diameter reduction (mm)	1.005	0.951	0.468	0.674
Standard deviation of diameter reduction	0.227	0.211	0.217	0.290
New diameter (mm)	11.119	10.168	9.701	9.027
New diameter standard deviation	0.227	0.277	0.244	0.223
Segment volume (mm^3)	228.582	202.950	95.407	127.765
Segment volume standard deviation	49.402	67.484	51.550	52.950

Compact 12-1 had an as-irradiated diameter of 12.256 mm, ±0.0086 mm (Stempien et al. 2016). Table 4 summarizes the compact diameter after each of the three segments of radial deconsolidation and the volume of compact material removed from each segment of Compact 12-1. Three radial deconsolidation segments were run; however, the compact fell off the rod while the apparatus was being positioned for video collection after the third segment. Using calipers, the compact was measured once at each of three locations along its length. Table 4summarizes the compact diameter after each of the three segments of radial deconsolidation and the volume of compact material removed from each segment of deconsolidation. LBL of the thimble material from the three radial segments has been completed and data analysis is in progress. The axial deconsolidation of the compact core has been completed, the axial thimble material has finished LBL, and LBL data analysis is in progress. Gamma surveys of particles from each of the axial and radial thimbles have not yet begun.

Table 4. Summary of Compact 12-1 diameter change, new diameter after each segment of deconsolidation, and the volume of the compact material removed.

Parameter	Segment 1	Segment 2	Segment 3
Deconsolidation time	16	15.5	15
Diameter reduction (mm)	0.741	0.287	1.999
Standard deviation of diameter reduction	0.221	0.217	0.288
New diameter (mm)	11.515	11.227	9.229
New diameter standard deviation	0.222	0.279	0.258
Segment volume (mm^3)	172.438	53.004	389.440
Segment volume standard deviation	49.965	72.700	54.491

The as-irradiated diameter of Compact 12-3 was measured to be 12.254 mm, ±0.005 mm (Stempien et al. 2016). Compact 12-3 was inadvertently dislodged from the rod after the first radial deconsolidation step. The compact was then remounted to the rod (using the procedures and equipment used to mount it the first time), and video was obtained of the rotating compact. Remounting the compact was successful for purposes of measuring the compact after the first (and only) segment of radial deconsolidation; however, the mounting jig can only center an as-irradiated compact on the rod. The remounted compact would not be centered on the rod, and any subsequent radial deconsolidation steps would not remove material uniformly from the compact. Thus, no further radial segments were obtained for this compact. Table 5 summarizes the change in compact diameter and volume after the radial deconsolidation step. LBL was completed on thimble material collected from the radial deconsolidation step, and fission product analysis is in progress. Axial deconsolidation of the core is planned.

Table 5. Summary of Compact 12-3 diameter change, new diameter after a segment of deconsolidation, and the volume of the compact material removed.

Parameter	Radial Deconsolidation Segment 1
Radial deconsolidation time (min)	15
Diameter reduction (mm)	0.617
Diameter reduction standard deviation (± mm)	0.188
New diameter (mm)	11.637
New diameter standard deviation (± mm)	0.188
Segment volume (mm^3)	144.336
Segment volume standard deviation (± mm)	42.889

References

Collin, Blaise P., 2015a, *AGR-3/4 Irradiation Test Final As-Run Report*, INL/EXT-15-35550, Rev. 0, Idaho National Laboratory, June 2015.

Collin, B. P., 2015b, “AGR-3/4 Irradiation Experiment Test Plan,” PLN-3867, Rev. 1, Idaho National Laboratory.

Demkowicz, Paul A., 2017, “AGR-3/4 Phase 2 Post-Irradiation Examination Plan,” PLN-5382, Idaho National Laboratory, May 5, 2017.

Hawkes, Grant L., 2016, “AGR-3/4 Daily As-Run Thermal Analyses,” ECAR-2807, Rev. 1, Idaho National Laboratory, April 21, 2016.

Helmreich, G., F. C. Montgomery, and J. D. Hunn, 2015, *Development of a Radial Deconsolidation Method*, ORNL/TM-2015/699, Oak Ridge National Laboratory.

Hunn, J., M. P. Trammell, and F. C. Montgomery, 2011, *Data Compilation for AGR-3/4 Designed-to-Fail (DTF) Fuel Compact Lot (LEU03-10TOP2/LEU03-07DTF-OP1)-Z*, ORNL/TM-2011/124, Oak Ridge National Laboratory.

Scates, D. M., 2015, “Release-to-Birth Ratios for AGR-3/4 Operating Cycles 151A through 155B,” ECAR-2457, Rev. 1, Idaho National Laboratory, June 5, 2015.

Stempien, J. D., F. J. Rice, P. L. Winston, and J. M. Harp, 2016, *AGR-3/4 Irradiation Test Train Disassembly and Component Metrology Frist Look Report*, INL/EXT-16-38005, Idaho National Laboratory.

Stempien, J. D., 2017, *Radial Deconsolidation and Leach-Burn-Leach of AGR-3/4 Compacts 3-3, 12-1, and 12-3*, INL/EXT-17-43182, Idaho National Laboratory, September 2017.

Sterbentz, James W., 2015, “JMOCUP As-Run Daily Physics Depletion Calculation for the AGR-3/4 TRISO Particle Experiment in the ATR Northeast Flux Trap,” ECAR-2753, Rev. 1, Idaho National Laboratory, September 2015.

2.1.1.5 High-Temperature Heating Test of AGR-3/4 Compact 3-2

Introduction

AGR-3/4 Compact 3-2 was heated in the FACS furnace at 1600°C for 330 hours before ramping to 1700°C for 48 hours. A detailed test plan is available from (Stempien 2017). Fabrication parameters and elements of the irradiation history specific to AGR-3/4 Compact 3-2 are listed in Table 6. For Capsule 3, analysis of fission gas release during the irradiation indicated that it is most likely that all of the DTF particles in the capsule failed (20 in each compact) (Scates 2015). Thus, 20 failed DTF particles were expected to be present in Compact 3-2 at the start of the heating test.

Table 6. Selected fuel fabrication and irradiation properties for Compact 3-2.

Compact[a]	3-2
Fuel compact fabrication identification[b]	(LEU03-10T-OP2/LEU03-07DTF-OP1)-Z040
Burnup (%FIMA)[c]	12.49
Fast fluence (n/m^2, E > 0.18 MeV)[c]	4.17×10^{25}
TAVA irradiation temperature (°C)	1196
TA peak irradiation temperature (°C)[d]	1240
TA minimum irradiation temperature (°C)[d]	1154

[a] X-Y naming convention denotes location in irradiation test train: Capsule-Level (Demkowicz 2017).

[b] From Collin 2015 and Hunn, Trammel, and Montgomery 2011.

[c] Based on physics calculations (Sterbentz 2015). FIMA = fissions per initial metal atom.

[d] TA = Time-averaged temperature, determined from thermal calculations (Hawkes 2016).

Preliminary Condensation Plate Data

The FACS furnace features a water-cooled cold finger that extends down into the furnace chamber and resides just above the sample. A condensation plate is fixed on the end of the cold finger and kept at temperatures <150°C to provide a relatively cool surface for condensable fission products to deposit. Condensation plates are exchanged throughout the heating test and analyzed to determine the activity of fission products collected on each plate. Once removed from the FACS furnace, the condensation plates were counted at the HOG station. The activities measured on the plates were decay corrected back to the end of irradiation (EOI) plus 1 day (April 13, 2014, 5:00 a.m.). The activities were also adjusted according to previously determined experimental collection efficiencies for the plates. The measured activities of each isotope detected on condensation plates were then compared to the activities generated in the compact during irradiation, as predicted by physics calculations at EOI plus 1 day (Sterbentz 2015).

Figure 6 shows the Ag-110m release from Compact 3-2. The silver behavior is consistent with prior AGR-1 and AGR-2 heating tests: a relatively significant fraction of the inventory (i.e., significantly greater than a single particle inventory) is released rapidly near the start of the heating test, followed by negligible additional release at the isothermal hold temperature. In AGR-1 and AGR-2 1600 and 1700°C testing of compacts containing no exposed kernels, it was concluded that this release was dominated by inventory that resided in the compact outside of intact SiC (either in the OPyC layers or matrix) that was driven out of the compact at the elevated heating test temperature. In the heating test of AGR-3/4 Compact 3-2, the total Ag-110m release at the end of the test was equivalent to the 2.38 single particle inventories (compact fraction of 1.26E–3). Therefore, it appears likely that this release was from a similar mechanism as observed in previous AGR compact safety tests (release from OPyC or matrix inventory), and that there was little contribution from the failed DTF particles. Additional testing (e.g., radial DLBL) of similar compacts from Capsule 3 in the as-irradiated state will allow the inventory of Ag-110m in the matrix to be estimated, and will aid in the interpretation of the data from this heating tests. The fact that little additional Ag-110m was released upon increasing the temperature to 1700°C suggests that the matrix inventory of silver was driven out of the compact during the initial rise to 1600°C, and that no additional inventory was available for release from the DTF particles.

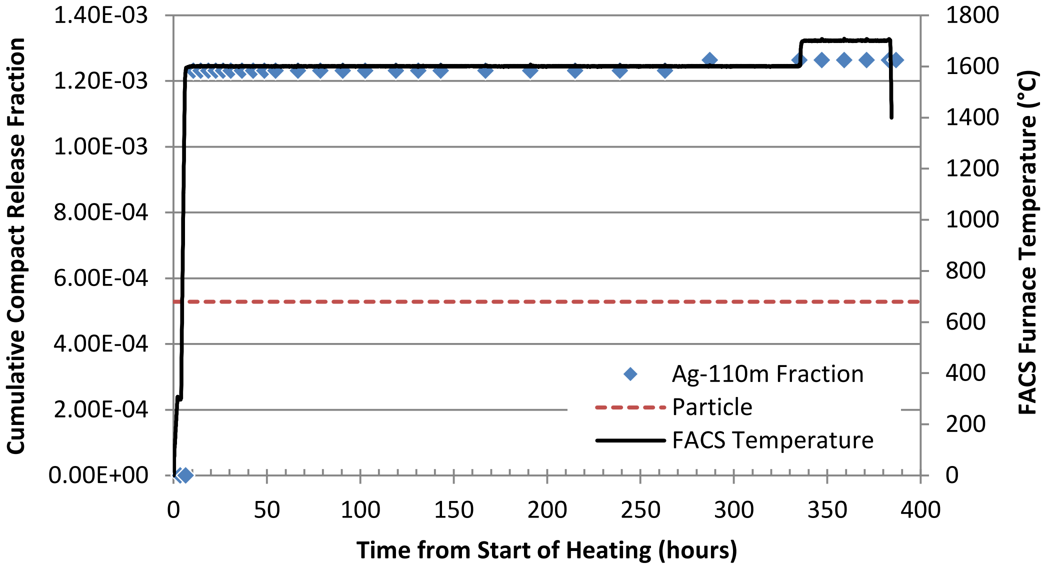

Figure 6. Ag-110m fractional release versus heating time. One particle inventory is equivalent to a fraction of 5.29E−4.

Figure 7 shows the Cs-134 release during the test. Following the initial high rate of Cs-134 release, the rate decreased significantly, reaching a nearly constant value after approximately 100 hours. For the 330 hours at 1600°C, a compact fraction of 1.772E–4 (one-third of the inventory in a single particle) was released. During the 48 hour hold at 1700°C, an additional 3.025E–4 (57% of a single particle inventory) was released. The total fractional release for the entire test was 4.797E–4 (90.6% of a single particle inventory). Since 20 DTF particles were in Compact 3-2, but only 90% of a single particle inventory of cesium was detected during the heating test, it can be concluded that the DTF particles released nearly all of their cesium during the AGR-3/4 irradiation in ATR (matrix retention of caesium at these irradiation temperatures for these irradiation durations is not expected to be significant).

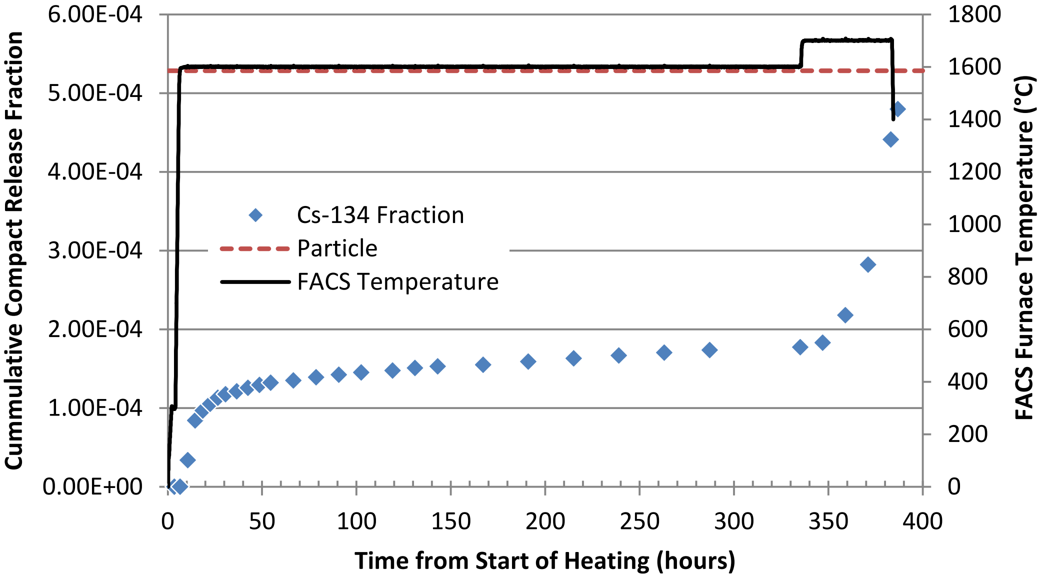

Figure 7. Cs-134 fractional release versus heating time. One particle inventory is equivalent to a fraction of 5.29E−4.

Figure 8 shows the Eu-154 fractional release during the heating test. Again, the Eu-154 behavior is consistent with previous heating tests of AGR-1 and AGR-2 fuel (neither of which had DTF particles). The europium release is gradual and highly temperature dependent. Based on the similarity with data from safety tests of compacts with intact TRISO particles, it is possible that the release is dominated by the europium inventory that built up in the compact matrix during the irradiation. However, it is not possible to discount the contribution of release from exposed DTF kernels. Additional testing of as-irradiated compacts will enable the matrix inventory at the EOI to be quantified and help interpret the heating test data. During the 330 hours at 1600°C, a europium fraction of 5.08E−3 (11 particle inventories) was released from the compact. During the 48 hour hold at 1700°C, an additional fraction of 2.6E−3 was released. The total europium fraction released by the end of the heating test was 7.69E−3 (14.5 particle inventories).

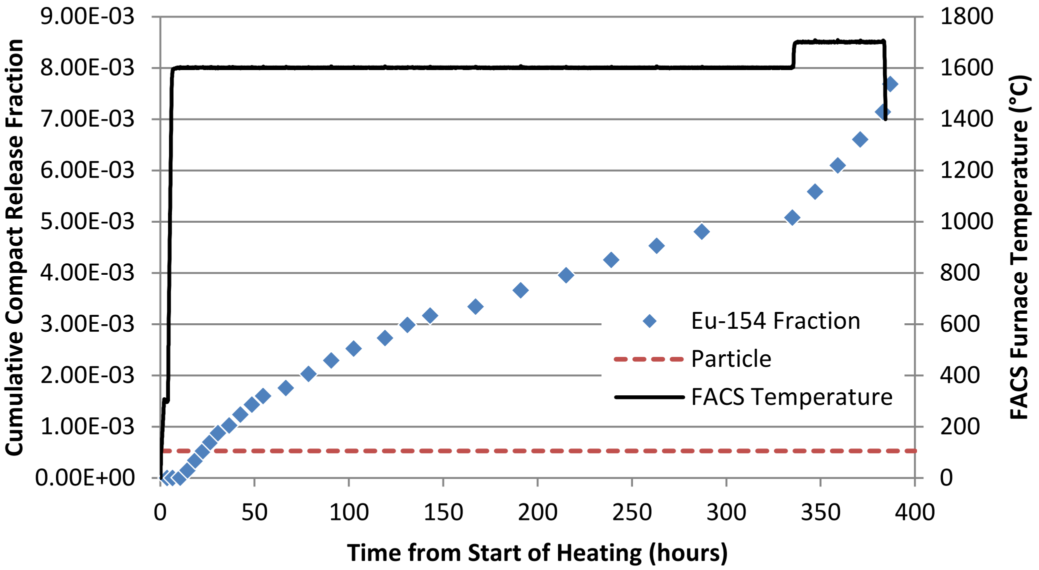

Figure 8. Eu-154 fractional release versus heating time. One particle inventory is equivalent to a fraction of 5.29E−4.

References

Collin, B. P., 2015, “AGR-3/4 Irradiation Experiment Test Plan,” PLN-3867, Rev. 1, Idaho National Laboratory.

Demkowicz, Paul A., 2017, “AGR-3/4 Phase 2 Post-Irradiation Examination Plan,” PLN-5382, Idaho National Laboratory, May 5, 2017.

Hawkes, Grant L., 2016, “AGR-3/4 Daily As-Run Thermal Analyses,” ECAR-2807, Rev. 1, Idaho National Laboratory, April 21, 2016.

Hunn, J., M. P. Trammell, and F. C. Montgomery, 2011, *Data Compilation for AGR-3/4 Designed-to-Fail (DTF) Fuel Compact Lot (LEU03-10TOP2/LEU03-07DTF-OP1)-Z*, ORNL/TM-2011/124, Oak Ridge National Laboratory.

Scates, D. M., 2015, “Release-to-Birth Ratios for AGR-3/4 Operating Cycles 151A through 155B,” ECAR-2457, Rev. 1, Idaho National Laboratory, June 5, 2015.

Sterbentz, James W., 2015, “JMOCUP As-Run Daily Physics Depletion Calculation for the AGR-3/4 TRISO Particle Experiment in the ATR Northeast Flux Trap,” ECAR-2753, Rev. 1, Idaho National Laboratory, September 2015.

Stempien, John D., 2017, “Test Plan for the 1600°C Heating Test of AGR-3/4 Compact 3-2,” PLN-5450, Idaho National Laboratory.

2.1.1.6 Advanced Microscopy Update on Kernel and TRISO Coating Analyses

UCO Kernel Examinations

Advanced microscopy imaging and data collection on UCO kernels of Particles AGR1-632-034, AGR1-433-001, and AGR2-223-R06 was completed at INL from July through September 2017 by a PhD candidate from the University of Florida. A preliminary summary of some data is provided below, although data interpretation, comparative evaluations, and recommendations are still to be performed.

Figure 9 shows the low-magnification, Z-contrast STEM image of lamellae from the center region of the fuel kernel from Particle AGR2-223-R06.. The microstructure features irregularly shaped pores, phases with a high average Z (bright contrasts), and phases with a relative low Z (in gray to dark contrasts). The area highlighted in the low-magnification image in Figure 9 (labeled AOI #1) is the area analyzed in Figure 10. The electron dispersive spectroscopy (EDS) line scan in Figure 10 from the area of interest (AOI #1) shows that the bright phase has an elevated uranium to oxygen atomic ratio compared to the dark phase. Additional EDS line scans (not included in this report) also indicate that the bright phase is slightly enriched with fission products of molybdenum, zirconium, and cadmium. The UCO fuel kernels are, in fact, heterogeneous mixtures of uranium oxide and uranium carbide, and these line scans are consistent with the character of the kernel mixture. The EDS line scan in Figure 11 clearly shows an increased xenon content in the selected gas bubble. However, to more accurately determine any other associated fission products in the fission gas bubble, electron energy loss spectroscopy elemental mapping should be used and a much thinner TEM specimen should be prepared. Due to the limitation of EDS detector, the measured contents of light elements, such as carbon, are extremely inaccurate, and the exact atomic ratio among U/C/O cannot be determined with EDS.

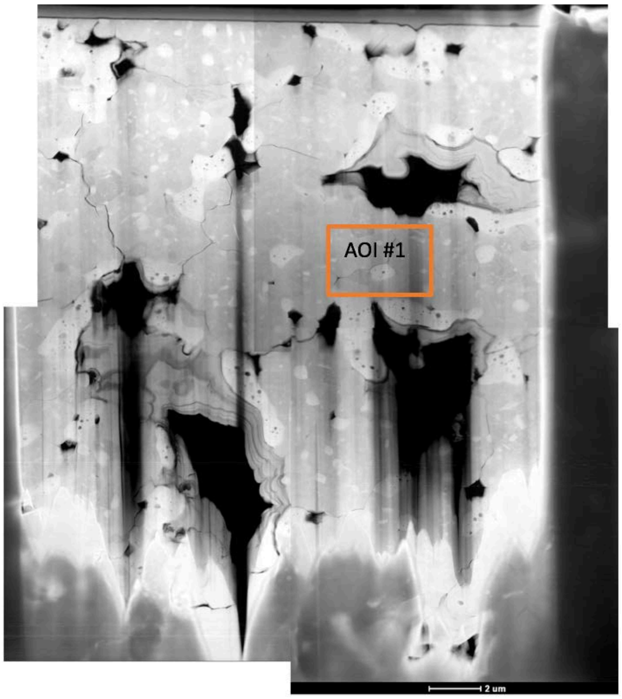

Figure 9. Overview Z-contrast STEM image from the center region from Particle AGR2-223-RS06.

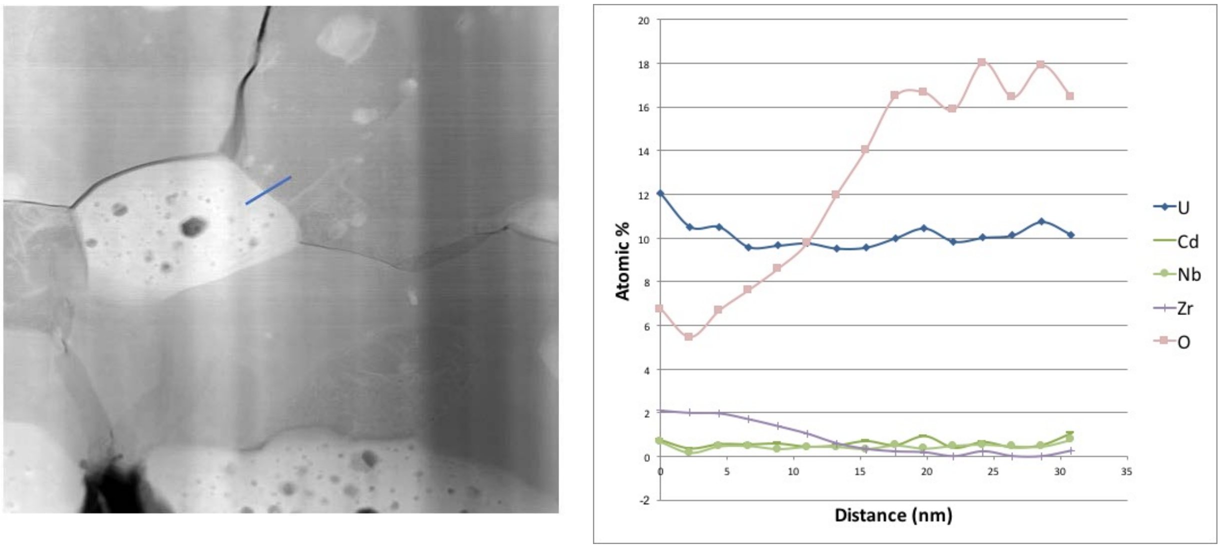

Figure 10. EDS line scan (short blue line) across the phase boundary showing a significant U/O ratio change (AOI #1)

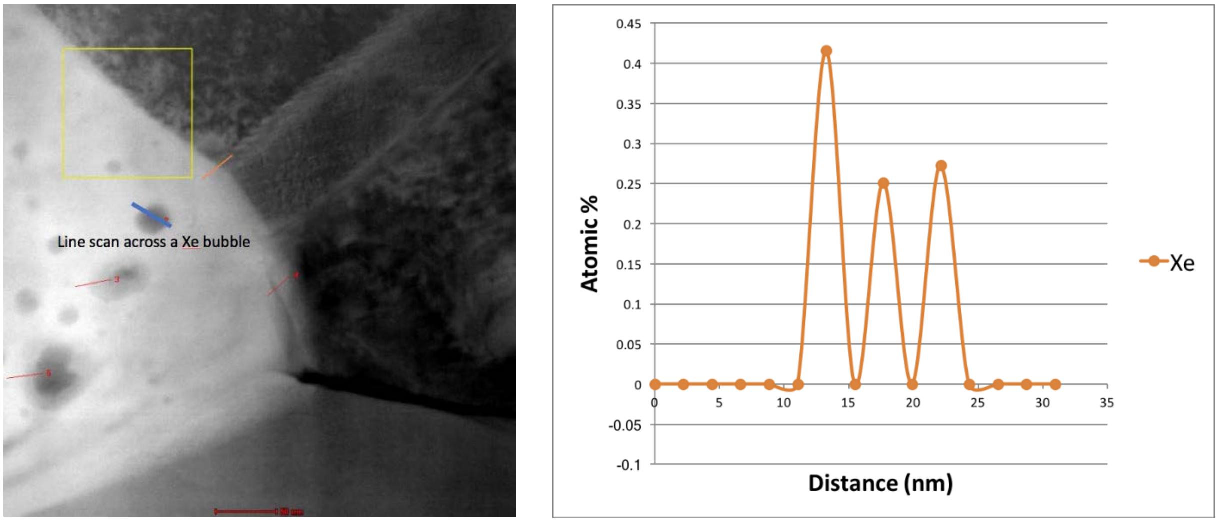

Figure 11. EDS line scan (short blue line) showing xenon in a gas bubble.

Scattered gas bubbles are also observed in the bright contrast phase of Particle AGR1-632-034. The EDS line scan (orange line) in Figure 12 also shows that the phase in a gray contrast contains a significant content of molybdenum.

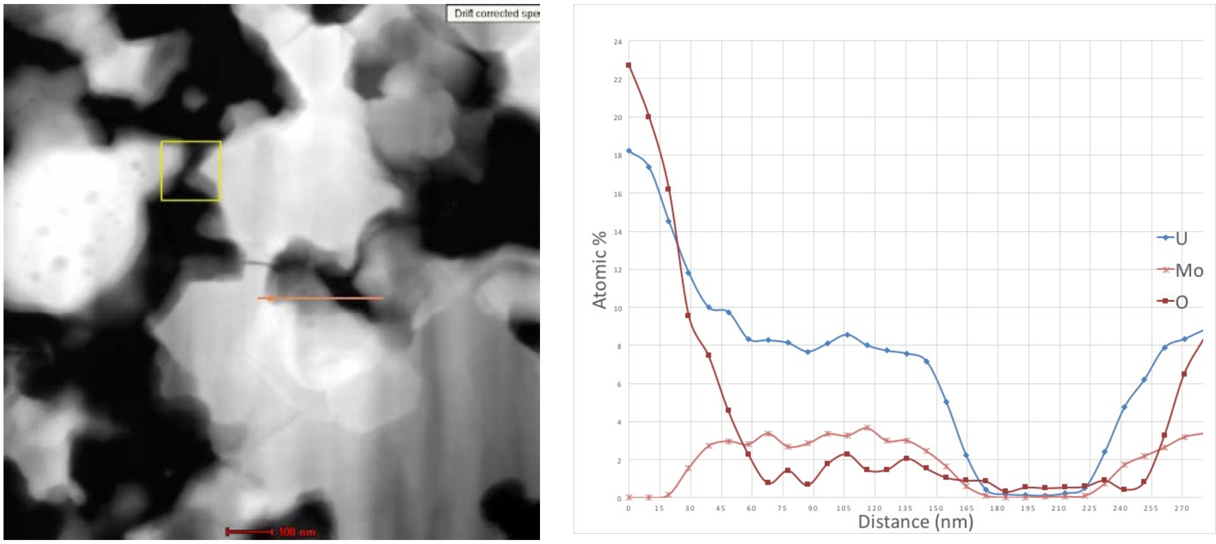

Figure 12. STEM image (left) showing the gas bubbles (dark phase) scattered in the high Z phase (bright phase) and the EDS line scan (right) showing enrichment of molybdenum in the gray contrast phase, and a possible pore or carbon precipitate in the dark contrast phase. Line scan was along the orange line in the STEM image.

2.1.1.7 Advanced Microscopy Focusing on AGR-2 TRISO Layers

Particle AGR2-223-RS06

Advanced microscopy data analysis was completed for this particle during July through September 2017, and a draft report was prepared. This report includes results from STEM, TEM, EDS, PED, and electron probe micro-analysis measurements. Integration and final interpretation of the results will be performed during October 2017. During analyses of lamellae from Particle AGR2-223-RS06, the position of the precipitates within the SiC layer was noted (e.g., whether a precipitate was located at grain boundaries or grain triple points). Additionally, during the previous analysis on the AGR-1 particles, very few micron-sized particles were analyzed; therefore, studies on the AGR-2 particles included more analysis on precipitates in this size range.

Precipitates from three areas, highlighted in Figure 13a, were analyzed. Taking the analyses of Area 2 (highlighted in the low-magnification image in Figure 13a and in the higher-magnification image in Figure 13c) as an example, a number of grain boundary precipitates were analyzed along with four large precipitates adjacent to Area 2. The locations of the EDS analysis points taken on the large precipitates near Area 2 are shown in Figure 14. The qualitative composition of the grain boundary fission product precipitates of Figure 13c and the EDS analysis point on the big precipitates, shown in Figure 14, are given in Table 7. The 11 grain boundary precipitates only exhibit significant amounts of palladium. The analysis of the EDS points on the large precipitates indicates the presence of palladium, uranium, and plutonium at all four analysis points. The palladium contents of these relatively large, micron-sized precipitates are significantly higher than those found in grain boundary precipitates. (Evaluation of the individual EDS spectra for BIG_PPTS_1_EDS and BIG_PPTS_2_EDS failed to support the presence of either zirconium or molybdenum at either of these locations.) Visual inspection of the individual EDS spectra for BIG_PPTS_2_EDS and BIG_PPTS_4_EDS could not unambiguously determine whether cerium was present at these locations.

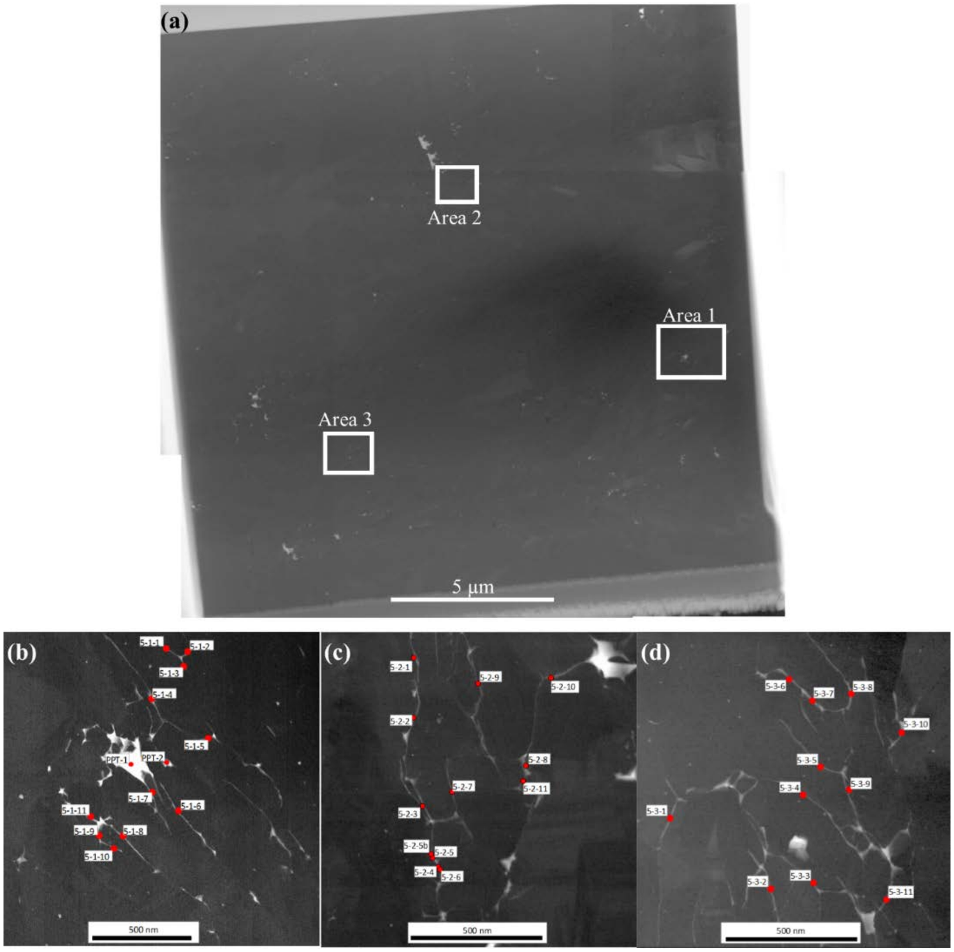

Figure 13. The locations of Areas 1, 2, and 3 on the Site 5 lamella are shown in (a) while the individual fission product precipitates that were analyzed with EDS are shown for Area 1 (b), Area 2 (c), and Area 3 (d).

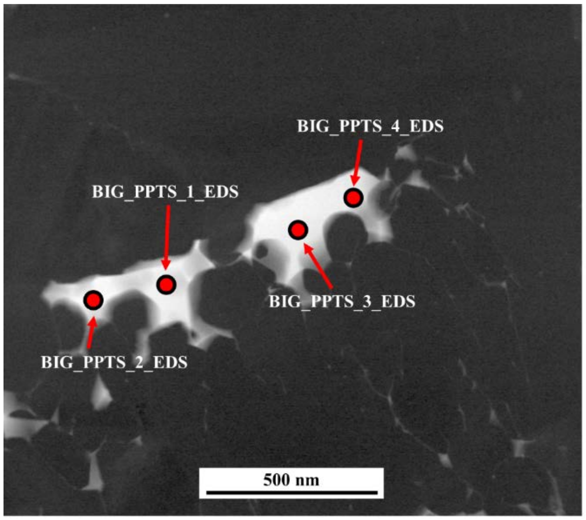

Figure 14. High-angle annular dark-field image showing the location of the EDS points on the large precipitates adjacent to Area 2.

Table 7. Composition of fission product precipitates from EDS analysis in Site 5, Area 2. Figure 13a shows the location of Area 2 within the Site 5 lamella. Figure 13c shows the grain boundary (GB) precipitates, and Figure 14 shows the large precipitates adjacent to Area 2.

	Summary of Elements Present at Precipitate Locations (atomic%)												
Precipitate	C	Si	Zr	Mo	Pd	Ag	Cd	Te	I	Cs	Ce	U	Pu
GB_1	46.54	49.11	0.00	0.00	4.21	0.09	0.00	0.00	0.00	0.00	0.02	0.00	0.00
GB_2	60.75	38.87	0.00	0.00	0.35	0.01	0.00	0.00	0.00	0.00	0.00	0.00	0.00
GB_3	60.82	37.13	0.02	0.00	1.93	0.00	0.08	0.00	0.00	0.00	0.00	0.00	0.00
GB_4	51.25	47.19	0.00	0.00	1.55	0.00	0.00	0.00	0.00	0.00	0.00	0.00	0.00
GB_5a	56.28	41.42	0.00	0.00	2.21	0.00	0.00	0.06	0.00	0.00	0.00	0.00	0.00
GB_5b	56.95	40.88	0.00	0.01	2.06	0.08	0.00	0.00	0.00	0.00	0.00	0.00	0.00
GB_6	66.76	32.46	0.00	0.00	0.74	0.00	0.00	0.00	0.01	0.00	0.00	0.00	0.00
GB_7	62.96	36.72	0.00	0.00	0.31	0.00	0.00	0.00	0.00	0.00	0.00	0.00	0.00
GB_8	57.98	39.98	0.01	0.00	1.82	0.16	0.00	0.00	0.02	0.00	0.00	0.00	0.00
GB_9	64.79	34.14	0.00	0.00	1.05	0.00	0.00	0.00	0.00	0.00	0.00	0.00	0.00
GB_10	59.73	39.29	0.00	0.00	0.95	0.00	0.00	0.00	0.00	0.00	0.00	0.01	0.00
GB_11	64.92	34.58	0.00	0.00	0.45	0.03	0.00	0.00	0.00	0.00	0.00	0.00	0.00
BIG_PPTS_1_EDS	40.47	30.23	0.28	0.00	20.71	0.00	0.00	0.00	0.00	0.00	0.05	6.00	2.23
BIG_PPTS_2_EDS	42.73	25.38	1.35	0.90	21.31	0.00	0.02	0.06	0.00	0.00	0.47	5.78	1.95
BIG_PPTS_3_EDS	41.08	26.73	0.03	0.00	23.54	0.00	0.00	0.00	0.00	0.00	0.14	6.29	2.15
BIG_PPTS_4_EDS	48.12	24.92	0.00	0.00	18.46	0.10	0.14	0.00	0.00	0.02	0.20	5.98	2.02

Particle AGR2-222-RS036

TEM lamella were fabricated from the SiC layer of TRISO Particle AGR2-222-RS036 according to the research plan shown in Figure 15. The particle exhibited debonding between the buffer and IPyC layers around the majority of the visible cross section of the particle. TEM lamellae in the SiC layer were selected from areas in the SiC layer that were adjacent to or as far removed as possible from the debonded region to assess the potential influence of the debonded buffer/IPyC layer on fission product transport behavior. Three TEM lamellae were taken from each location at “A” and “B” in Figure 15. The three lamellae collectively spanned the entire thickness of the SiC layer in each location and are referred to as inner, center, and outer samples where the inner lamella was taken from near the IPyC/SiC interface, the outer lamella was taken near the OPyC/SiC interface, and the center lamella was taken from the center region of the SiC layer. Fission product precipitates in three areas of each lamella in Location A were measured for composition using EDS (Figure 16). Due to the size of the precipitates versus the thickness of the lamella, the composition reported by the EDS analysis software can only be considered to be qualitative. Figure 17 is an example of the fission product precipitates that were analyzed with EDS with the associated SiC grain orientation images for Lamella 1, Area 1, from Particle AGR2-222-RS036. (Recall that Figure 15 shows the location of Lamella 1, and Figure 16 [left] shows the location of Area 1 within Lamella 1.) This work will continue in October 2017.

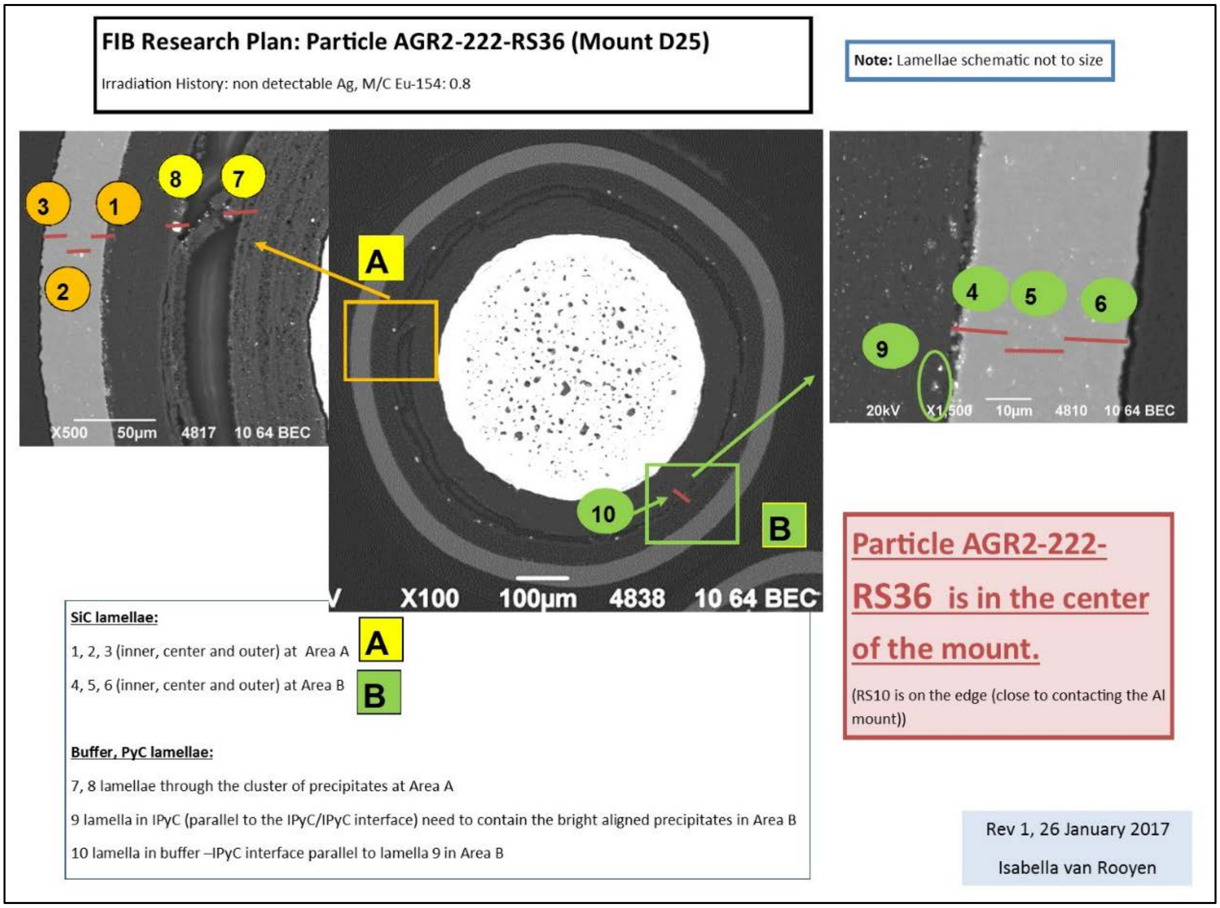
FIB Research Plan: Particle AGR2-222-RS36 (Mount D25)

Irradiation History: non detectable Ag, M/C Eu-154: 0.8

Note: Lamellae schematic not to size

SiC lamellae:

1, 2, 3 (inner, center and outer) at Area A

4, 5, 6 (inner, center and outer) at Area B

Buffer, PyC lamellae:

7, 8 lamellae through the cluster of precipitates at Area A

9 lamella in IPyC (parallel to the IPyC/IPyC interface) need to contain the bright aligned precipitates in Area B

10 lamella in buffer –IPyC interface parallel to lamella 9 in Area B

Particle AGR2-222-RS36 is in the center of the mount.

(RS10 is on the edge (close to contacting the Al mount))

Rev 1, 26 January 2017

Isabella van Rooyen

Figure 15. The research plan for the analysis of Particle AGR2-222-RS036.

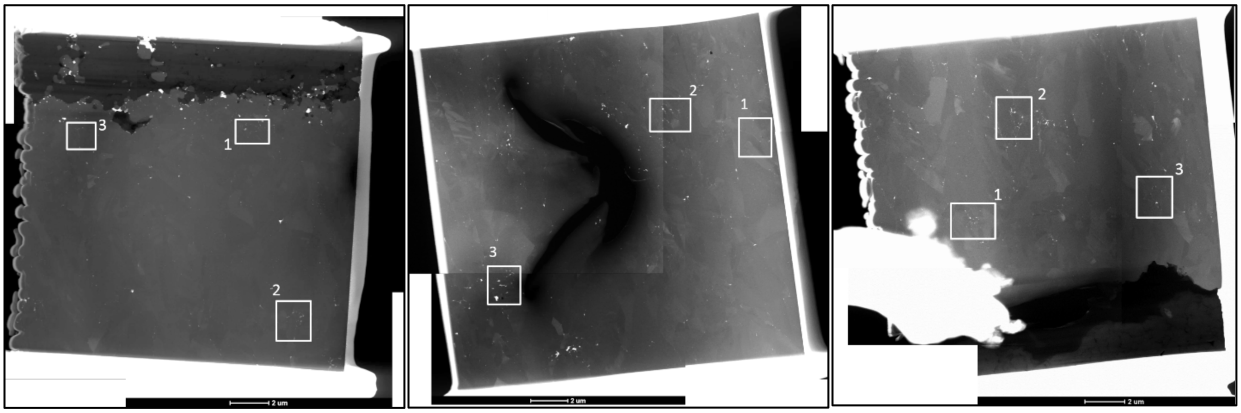

Figure 16. The three locations used for EDS and PED analysis on Lamellae 1 through 3 from Location A from Particle AGR2-222-RS036.

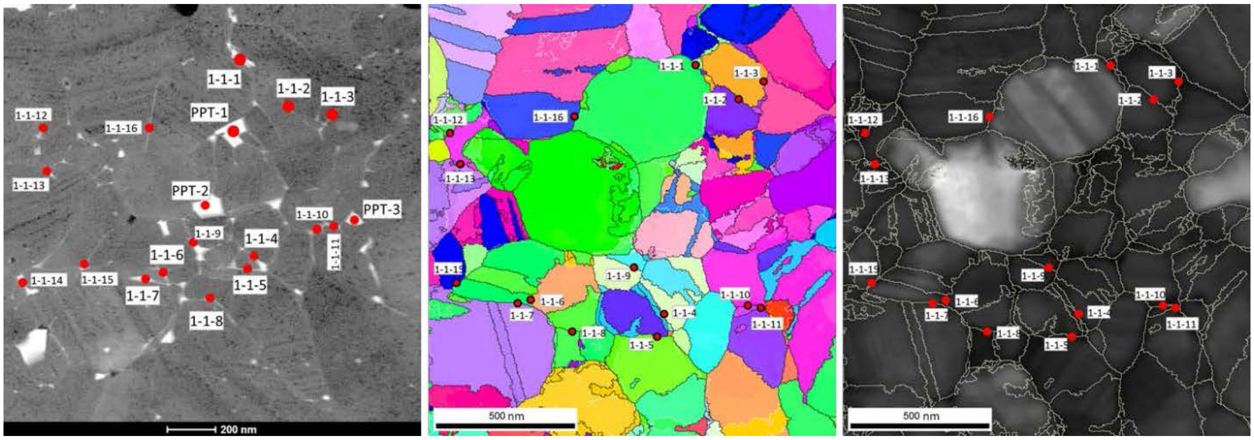

Figure 17. Fission product precipitates (left) that were analyzed with EDS and SiC grain orientation images (middle and right) for Lamella 1, Area 1, from Particle AGR2-222-RS036.

Neutron Irradiation Damage

During the fourth quarter of FY17, the TEM imaging for estimating distribution, volume fraction, and number density of irradiation induced voids in multiple lamellae of the SiC layers from Particles AGR1-632-034, AGR1-523-SP01, AGR1-131-066, AGR1-433-001, and AGR2-223-RS06, were completed. The data analysis process will be performed in the coming months. This work led to a significant finding on the formation of intragranular palladium precipitates at the metamorphed site of alpha-phase SiC within the bulk beta-phase SiC that comprises the majority of the SiC layer. These irradiation-induced low-temperature alpha-SiC precipitates were initially identified in Particles AGR1-632-034 and AGR2-223-RS06. No evidence of the localized alpha-SiC precipitates was found in unirradiated SiC (which is beta-phase SiC).

2.1.2 Safety Testing and Post-Irradiation Examination at ORNL

Table 8 is an update to the summary of AGR-2 compact safety testing in the CCCTF first presented and discussed in the 2017 first quarter report (INL 2017, pp. 13–19). For Compacts 2-3-2 and 3-4-1, the total fractional releases during safety testing are presented as approximate or to-be-determined values because measurement of the CCCTF deposition cup collection efficiency (needed to refine the accuracy of the results) has not been completed. Data from the safety test on AGR-2 UCO Compact 2-3-1 were finalized during the current reporting period and have been added to Table 8. Two additional safety tests on fuel compacts containing TRISO particles produced by Pebble Bed Modular Reactor, Ltd. in South Africa were also performed during the fourth quarter of FY17, but are not included here due to contract restrictions.

Table 8. AGR-2 safety tests. Bold type for Compact 2-3-1 indicates that these data were finalized in fourth quarter of FY17.

Compact ID	Fuel Type	Irradiation Temp. (TAVA[a]) (°C)	Average Burnup (%FIMA[b])	Safety Test Temp. (°C)	Failed SiC	Cs-134 Release	Ag-110m Release [c]	Eu-154 Release	Sr-90 Release
3-3-2	UO_2	1062	10.5	1600	≥6	2.1×10^{-3}	1.7×10^{-2}	3.8×10^{-4}	1.4×10^{-3}
3-4-2	UO_2	1013	10.7	1600	≥26	9.3×10^{-3}	1.1×10^{-2}	3.2×10^{-4}	2.7×10^{-3}
2-2-2	UCO	1287	12.6	1600	0	2.5×10^{-7}	7.3×10^{-3}	4.7×10^{-2}	4.1×10^{-2}
5-2-2	UCO	1141	12.3	1600	0	5.9×10^{-6}	1.7×10^{-2}	1.1×10^{-3}	7.9×10^{-4}
2-3-1	**UCO**	**1296**	**12.6**	**1600**	**0**	$\mathbf{4.0 \times 10^{-6}}$	$\mathbf{1.8 \times 10^{-2}}$	$\mathbf{8.4 \times 10^{-2}}$	$\mathbf{7.9 \times 10^{-4}}$

Compact ID	Fuel Type	Irradiation Temp. (TAVA[a]) (°C)	Average Burnup (%FIMA[b])	Safety Test Temp. (°C)	Failed SiC	Cs-134 Release	Ag-110m Release [c]	Eu-154 Release	Sr-90 Release
6-4-2	UCO	1018	9.3	1600	0	6.2×10^{-5}	3.4×10^{-3}	2.7×10^{-4}	8.7×10^{-5}
5-4-1	UCO	1071	12.1	1800	1–2	1.0×10^{-4}	1.7×10^{-1}	6.0×10^{-3}	2.3×10^{-3}
2-3-2	UCO	1296	12.7	1800	1–2	$\sim 3 \times 10^{-4}$	$\sim 2 \times 10^{-2}$	$\sim 2 \times 10^{-1}$	TBD
3-4-1	UO_2	1013	10.6	1700	High	$\sim 9 \times 10^{-2}$	$\sim 8 \times 10^{-2}$	TBD	TBD

[a] TAVA irradiation temperature is based on thermal calculations [Hawkes 2014, Table 4].

[b] FIMA is based on physics calculations [Sterbentz 2014, Table 6].

[c] Safety test release fractions are based on the net amount of each isotope generated by the irradiation and do not account for any release during irradiation; Ag-110m release during irradiation was significant from UCO compacts and must be considered to correctly interpret data.

[d] Compact 3-4-1 safety test was terminated after 162 hours at 1700°C due to high release, other tests were run for approximately 300 hours at test temperature.

The three listed compacts with an identification number beginning with “2” were from AGR-2 Capsule 2 and irradiated at a significantly higher temperature than compacts from the other capsules in the AGR-2 test train. The elevated irradiation temperature in Capsule 2 resulted in significantly more europium and strontium diffusion through intact SiC during the irradiation test. AGR-1 PIE and safety testing has shown that europium and strontium are mostly trapped by the surrounding OPyC and matrix graphite after passing through the SiC during the irradiation test, and are then slowly released from the OPyC and matrix graphite when irradiated compacts are heated to 1600 to 1800°C during safety testing. Table 8 shows significantly higher releases of Eu-154 and Sr-90 from Compacts 2-3-1 and 2-2-2 (compared to releases from safety testing of compacts irradiated at lower temperatures in other capsules) due to the higher level of these isotopes in the Capsule 2 compact OPyC and matrix at the start of the safety test. Compact 2-3-2 exhibited even higher releases due to the high concentrations of Eu-154 and Sr-90 in the OPyC and matrix combined with additional diffusion through the SiC while at 1800°C. In contrast, the UO_2 compacts listed in Table 8 showed two orders of magnitude lower Eu-154 and Sr-90 release during 1600°C safety testing than was observed from safety testing UCO compacts at 1600°C. Europium and strontium exist as carbides in the irradiated UCO-TRISO system and as oxides in the UO_2-TRISO system [McMurray et al. 2017]. The carbide form is not as well retained by the kernel and TRISO coatings as the oxide form.

Table 9 shows the distribution of europium and strontium within the CCCTF furnace after it was released by Compact 2-3-1. The europium and strontium retention characteristics of graphite are further demonstrated by the fact that a large fraction of the europium and strontium released from the compact at 1600°C was still residing in the encapsulating graphite holder at the end of the safety test.

Table 9. Radioactive isotope distribution on furnace internal components after the Compact 2-3-1 1600°C safety test.

Component	Sr-90	Ag-110m	Cs-134	Eu-154	Eu-155
Deposition cups	50.6%	100%	80.6%	22.1%	19.4%
Tantalum parts	12.7%	~0%	19.4%	12.5%	13.1%
Graphite holder	36.7%	~0%	~0%	65.5%	67.6%

^{137}Cs is not reported for Compact 2-3-1 because it was too low to measure above background contamination.

Release of Kr-85 was very low (below the detection limit of 7 × 10^{-7}) and this indicates no particles had through-layer failure of all three gas tight layers (IPyC, SiC, and OPyC). The cumulative amount of Cs-134 collected on the deposition cups during the Compact 2-3-1 safety test was less than 2% of the Cs-134 inventory in one particle and at a level that was likely dominated by hot cell contamination. Based on this very low cesium collection, it can be concluded that no particles experienced SiC failure during safety testing, which would typically release more than ten times the collected level of cesium.

The estimated time-dependent safety test releases from AGR-2 UCO Compact 2-3-1 are shown in Figure 18. The general trends were comparable to what was observed in the other AGR-2 and AGR-1 UCO fuel safety tests at 1600°C. Silver, which is not retained well by graphite at safety test temperatures, exhibited the typical rapid fractional release as the furnace reached test temperature followed by insignificant additional release. Europium and strontium release was more gradual, and this is attributed to slow release of fission products trapped in the OPyC and matrix graphite that had been previously released through intact SiC during the irradiation, as discussed above. Figure 19 shows the average fractional release rate to each CCCTF deposition cup. The rate of silver release dropped as the silver trapped in the OPyC and matrix graphite was depleted. No Ag-110m was detected on the deposition cups after the third cup, which was removed after the compact had been held for approximately 15 hours at 1600°C. The rate of europium and strontium collection on the deposition cups was relatively constant after the compact had been at 1600°C for a sufficient period to reach a steady state of release from the graphite holder. The collection rate for Cs-134 increased as the furnace was raised to 1600°C and then leveled off as cesium contamination was apparently flushed from the system. After approximately 62 hours at 1600°C, the cesium collection on the deposition cups was at or below the detection threshold.

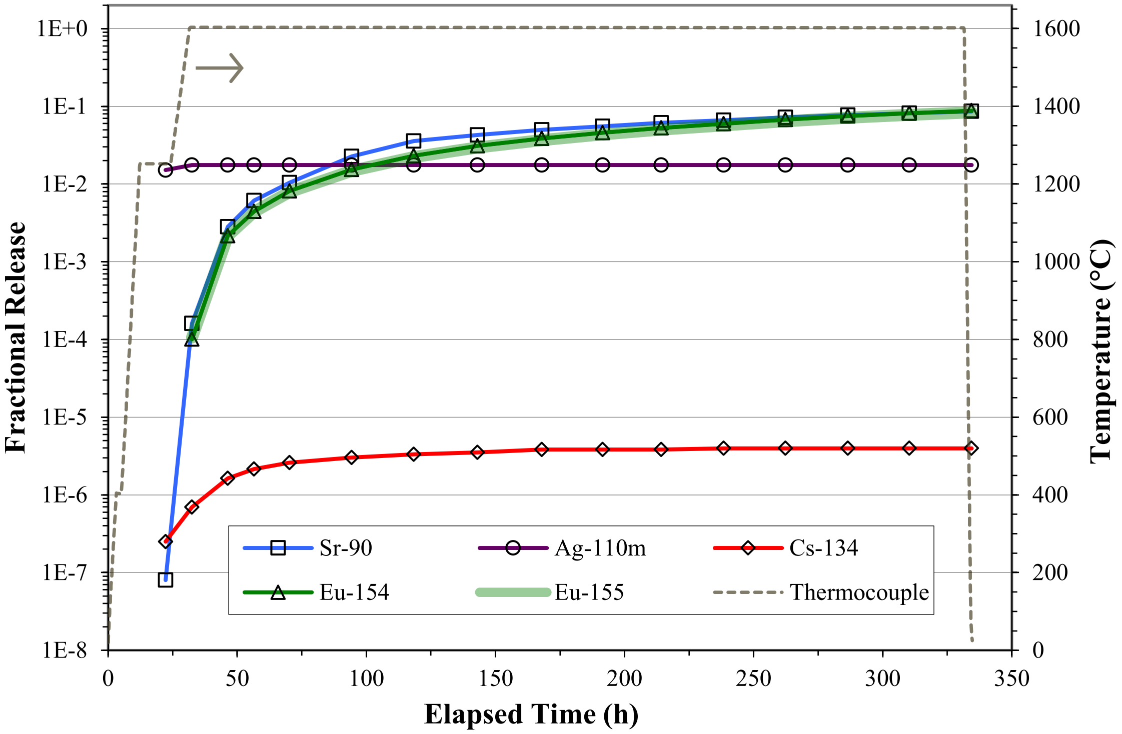

Figure 18. AGR-2 Compact 2-3-1 heating results (a compact fraction of 3.2 × 10^{-4} is equivalent to one particle inventory).

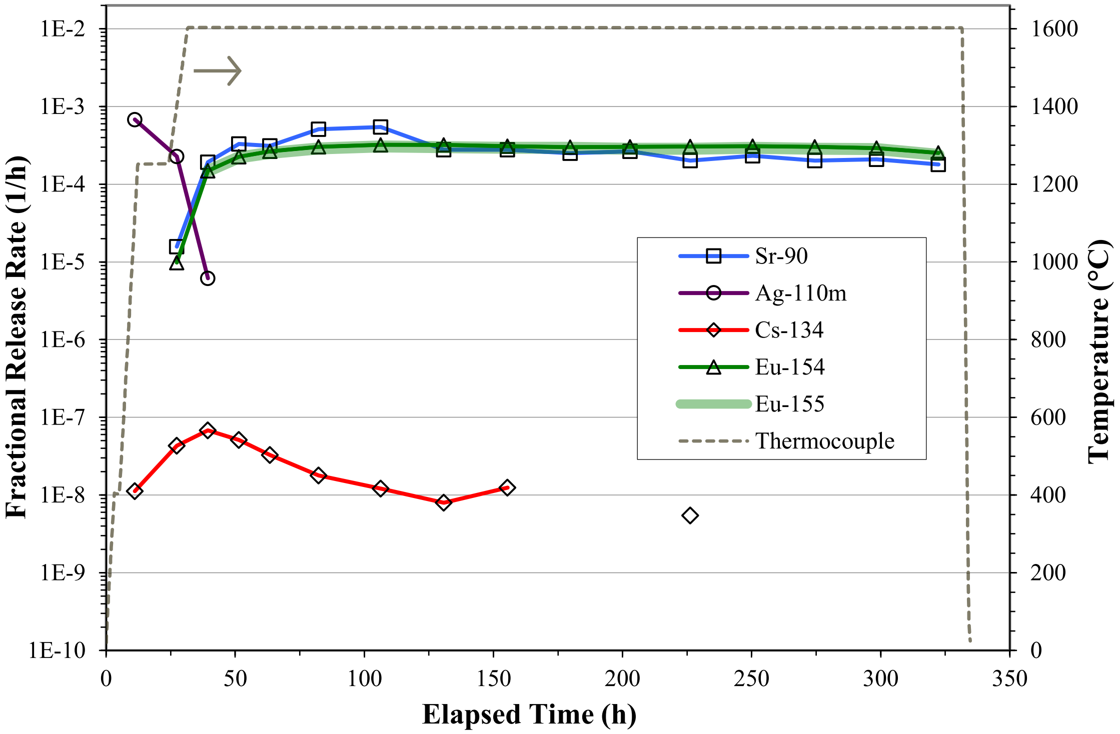

Figure 19. Rate of fission product release from Compact 2-3-1 during safety testing to 1600°C (data points with no measurable release rate are not plotted).

Further information on the 1600°C safety test of AGR-2 UCO Compact 2-3-1 are reported in ORNL/TM-2017/439 (Hunn et al. 2017), with comparison to the 1600°C safety tests of AGR-2 UCO Compact 2-2-2 (similar irradiation conditions) and AGR-2 UCO Compact 5-4-1 (similar burnup but approximately 150°C lower irradiation temperature).

References

Hawkes, G. L, 2014, “AGR-2 Daily As-Run Thermal Analyses,” ECAR-2476, Rev. 1, Idaho Falls, Idaho: Idaho National Laboratory.

Hunn, J. D., R. N. Morris, C. A. Baldwin, Z. M. Burns, F. C. Montgomery, and D. J. Skitt, 2017, *Safety-Testing of AGR-2 UCO Compacts 6-4-2 and 2-3-1,* ORNL/TM-2017/439, Rev. 1, Oak Ridge National Laboratory.

INL, 2017, *Advanced Reactor Technologies (ART): Very High Temperature Reactor (VHTR) Research and Development (R&D) Quarterly Report*, INL/LTD-17-40897, Idaho National Laboratory, 2017.

McMurray, J. W., T. B. Lindemer, N. R. Brown, T. J. Reif, R. N. Morris, and J. D. Hunn, 2017, “Determining the minimum required uranium carbide content for HTGR UCO fuel kernels,” *Annals of Nuclear Energy*, Vol. 104, 2017, pp. 237–242.

Sterbentz, J. W., 2014, “JMOCUP As-Run Daily Depletion Calculation for the AGR-2 Experiment in the ATR B-12 Position,” ECAR-2066, Rev. 2, Idaho National Laboratory.

2.1.3 Nuclear Data Management and Analysis System

B. Pham, N. Lybeck, G Hawkes and J. Einerson submitted to the “Best Estimate plus Uncertainty” International conference in Lucca, Italy (May 13–18, 2017) an abstract entitled “Uncertainty Quantification of Calculated Fuel Temperatures for the AGR-3/4 Irradiation Experiment.”

2.2 High-Temperature Materials

2.2.1 Alloy 617 Notch Testing

2.2.1.1 Base Metal Testing. During fourth quarter of FY17, three U-notch creep rupture tests were finished, a large radius test at 750°C, 145 MPa and two small radius test at 900°C, 36 MPa and 800°C, 80 MPa. Two additional tests were started and are currently ongoing, one large- and one small-radius U-notch test, each at 1000°C, 20 MPa. An updated Larson-Miller plot, which graphs stress versus the Larson-Miller parameter (a parameter that combines both rupture life and temperature), is shown in Figure 20. An arrow indicates that the 750°C, 145 MPa small-radius U-notch test is ongoing and will continue to shift towards the right until the specimen ruptures. As the 1000°C tests have not progressed significantly, they have not been included in the Larson-Miller plot. The large-radius U-notch tests continue to fall in line with the standard straight gauge specimens tested previously at INL, though the rupture life of the test at 750°C was longer than expected. The small-radius U-notch tests continue to demonstrate longer rupture lives than previously seen in the straight gauge testing. The small-radius 750°C test is the extreme case, which is beginning to extend beyond even the scatter of the compiled Larson-Miller data. The individual creep curves for each of the tests are shown in Figure 21. As seen in Figure 21a, the small-radius 750°C test maintains a relatively low creep rate and is expected to have significant life remaining, if it follows a similar curved behavior as the large-radius test shown in Figure 21b.

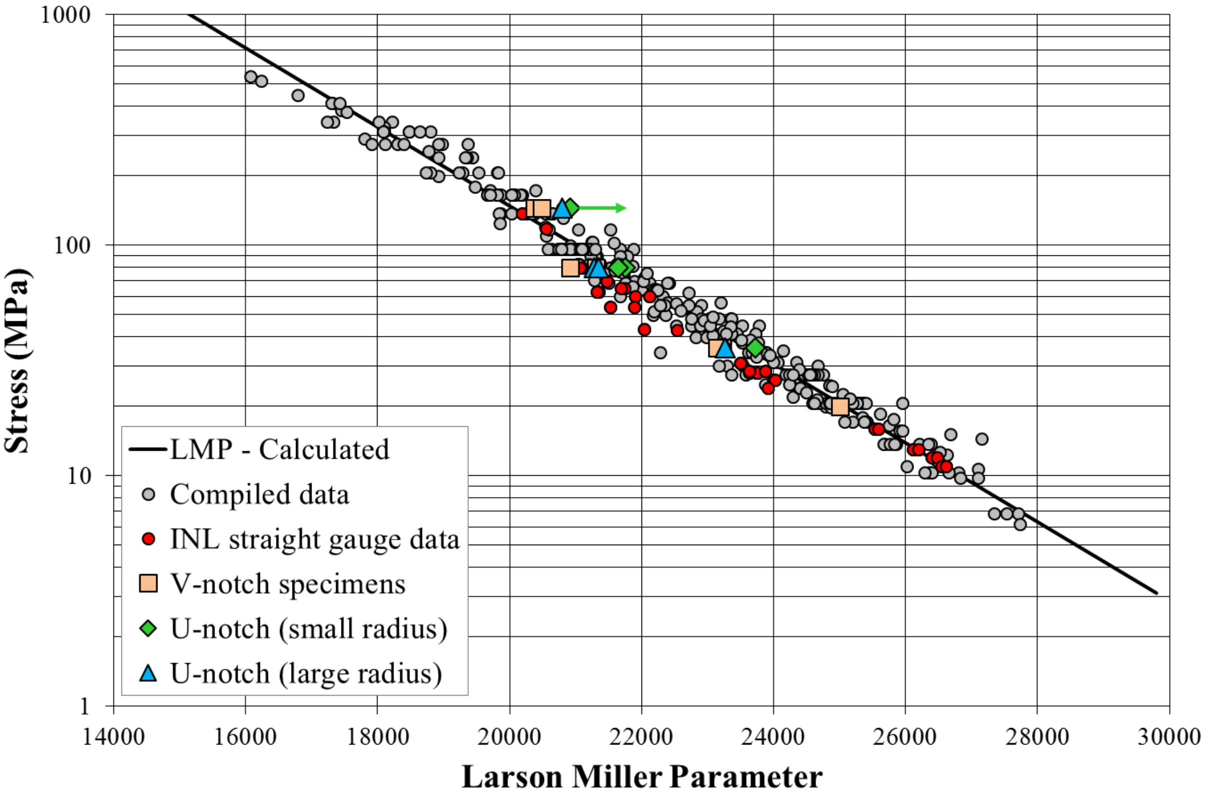

Figure 20. Larson-Miller plot summarizing all Alloy 617 creep rupture tests performed at INL.

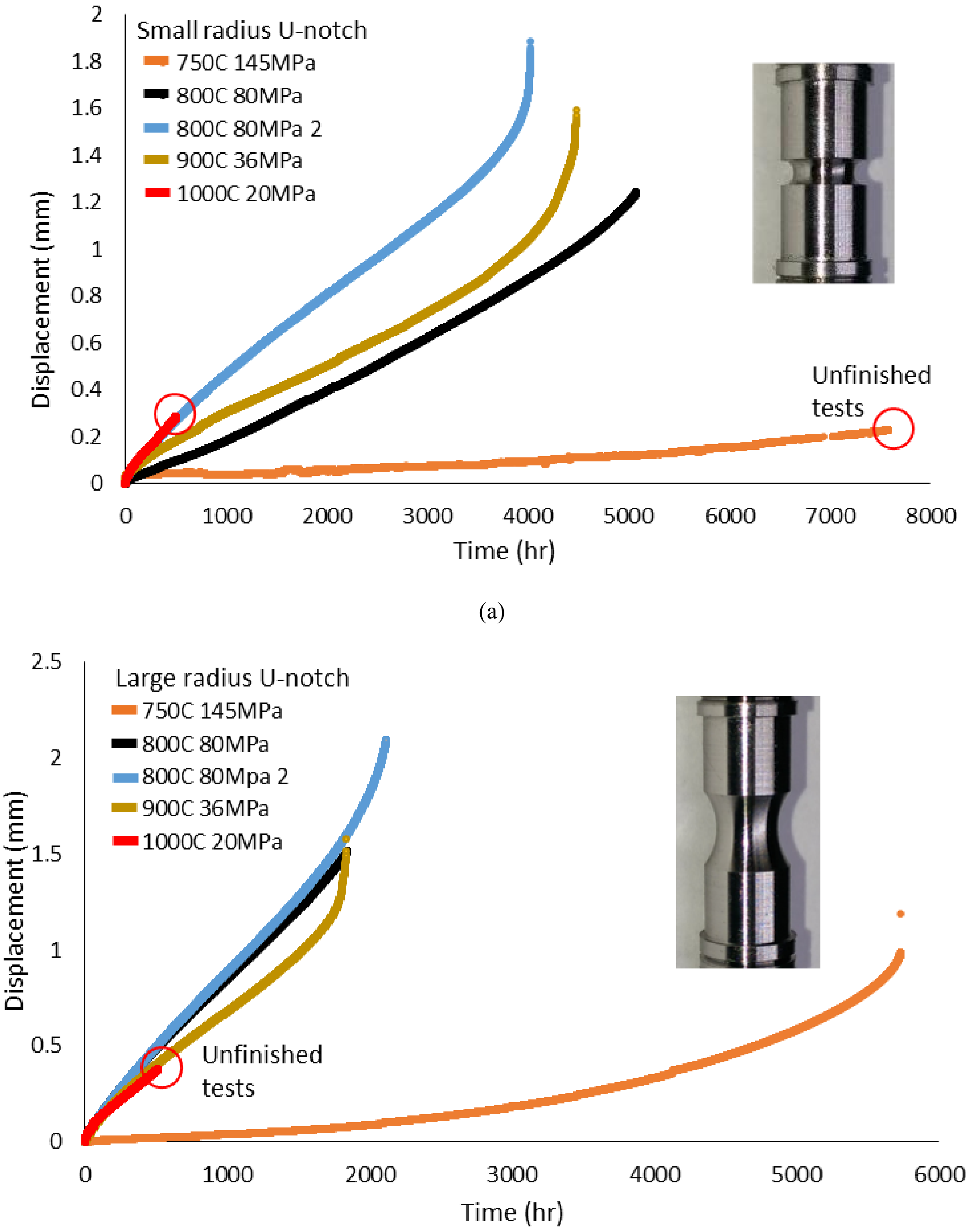

(a)

(b)

Figure 21. Individual creep curves for all Alloy 617 U-notch base metal tests performed at INL, showing (a) small-radius and (b) large-radius notch specimen results.

Each base metal specimen contains two identical notches, such that failure will occur at one notch, leaving the second notch unruptured (though near the rupture point) for metallographic analysis. Micrographs of the unruptured notches from recently finished tests are shown in Figure 22. These micrographs confirm what has been observed previously, that the large-radius U-notch specimens tend to exhibit damage through the thickness of the specimens (similar to a standard straight gauge creep specimen), whereas the damage in the small-radius U-notch specimens is significantly more sever near the notch tips, where stress and multi-axial stress states are the most severe. It was also observed, particularly in the 800°C, 80 MPa large-radius test (Figure 22b), that a significant number of creep damage locations occurred at grain boundaries approximately 45 degrees to the tensile axis, rather than the expected 90 degrees (perpendicular) as expected. This phenomena has been observed in simulations being performed at Argonne National Laboratory, but currently there is no clear explanation as to its cause.

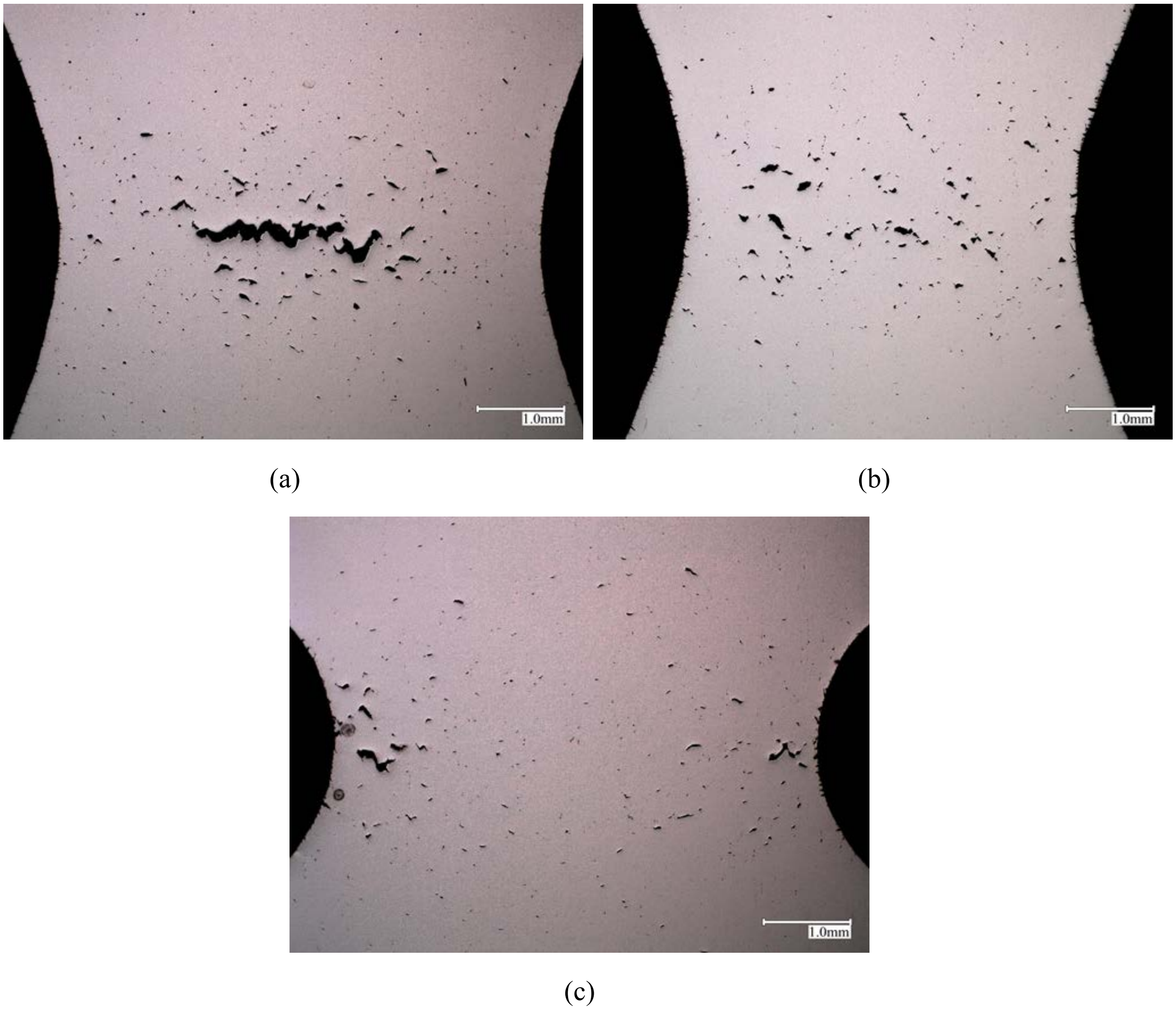

(a) (b)

(c)

Figure 22. Micrographs showing cross sections of the unruptured notches of specimens tested at (a) 750°C, 145 MPa—large radius, (b) 800°C, 80 MPa—large radius, and (c) 800°C, 80 MPa—small radius.

2.2.1.2 Weld Metal Testing. An interrupted creep test of a large-radius U-notch welded 617 specimen, tested at 800°C, 80 MPa, was completed fourth quarter of FY17. The test was performed to 800 hours to allow for observations of creep rates, as well as metallographic analysis, without extensive amounts of time for the first specimen tested. The metallographic analysis was particularly important to confirm that the location of the notch was within the weld metal as desired, which was confirmed, as shown in Figure 23. At the point of interruption, no creep damage was observed in the cross section of the notch. Figure 24 shows the displacement over time of the weld metal and base metal large-radius U-notch specimens tested at 800°C, 80 MPa. The weld metal was observed to experience a very low creep rate, when compared to the base metal.

Figure 23. Etched cross section of the weld metal large-radius U-notch interrupted creep test performed at 800°C, 80 MPa to 800 hours.

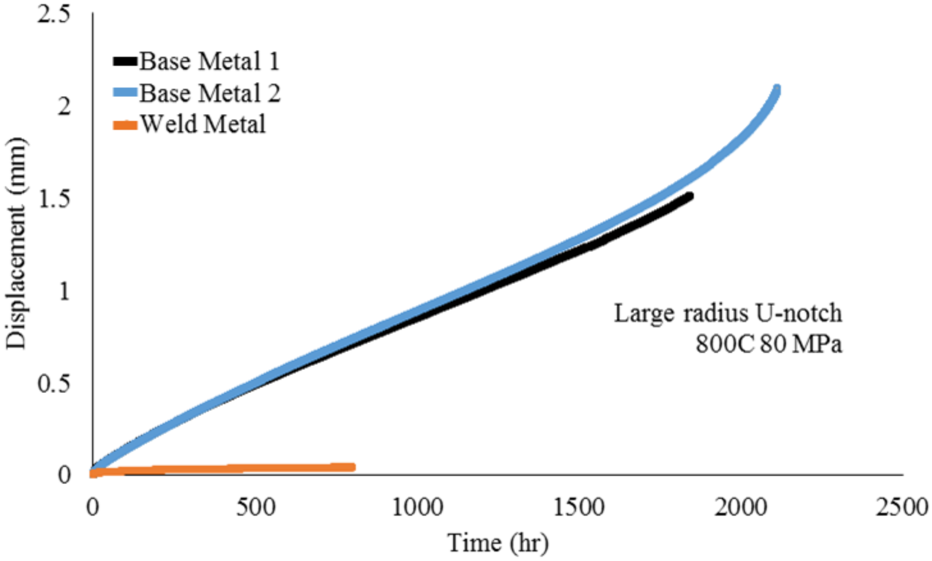

Figure 24. Comparison of creep rates of the recently tested weld metal large-radius U-notch specimen to the previously tested base metal specimens at identical conditions.

2.2.2 Alloy 617 High-Temperature Code Case

Sections of the Alloy 617 High-Temperature Code Case dealing with allowable stresses and physical properties were approved by letter ballot by ASME Section III Subgroup on Elevated Temperature Design and Subgroup on High Temperature Reactors. ASME Section III Subgroup on Materials, Fabrication and Evaluation and ASME Section II Subgroup on Non-Ferrous Alloys were briefed at Code Week on the continents of these sections and methods of analysis that were used to determine the specific numerical value of the relevant properties. These two subgroups are now balloting these sections of the code case.

The design fatigue curves were balloted by ASME Section III Working Group Creep-Fatigue and Negligible Creep and Working Group Fatigue Strength. The later working group did not pass the ballot due to a large number of members either abstaining or not returning ballots. A presentation was made to this Working Group at the August Code Week and the design fatigue curves were passed by a unanimous voice vote after the presentation. This section of the code case is now being balloted at the ASME Section III subgroup level.

2.3 Graphite Development and Qualification

2.3.1 Materials—Graphite

2.3.1.1 Graphite Baseline Program. A significant milestone was achieved for the ART Graphite research and development (R&D) baseline activity by completing the remaining material property testing of five different nuclear graphite billets. The baseline activity is generating an extensive amount of quantitative unirradiated material property test data for the graphite grades currently under consideration within the Graphite R&D Program. This unirradiated test data will be analyzed to determine the inherent variability of the material properties within the billets of as-produced nuclear graphite, within a single batch of billets, and from batch-to-batch.

Testing was completed for billets representing four different nuclear grades; 1 billet each of NBG-17, NBG-18, and IG-110 and two billets of PCEA. All material property test data was compiled in five different Engineering Calculations and Analysis reports (listed in Table 10) and delivered to the NDMAS database. These reports contain the measured test results but are not an analysis of property characteristics, as illustrated in Figure 25. The reports are an acceptance of the test methods used, data calculations and conversions being carried out, and review of the measured material property values from the standpoint of determining any anomalous behavior. The data within these reports represent over 7700 NQA-1 qualified graphite property measurement values and will be transferred to the Generation IV Information Forum (GIF) Handbook to allow dissemination of the data with the GIF partner countries.

Table 10. Graphite billets submitted to NDMAS in FY17.

Graphite Type	Billet No.	Report No.
PCEA	XPC02S8-7	ECAR-3725
NBG-18	635-4	ECAR-3726
IG-110	089052-7	ECAR-3621
NBG-17	830-3	ECAR-3727
PCEA	XPC01D3-36	ECAR-3677

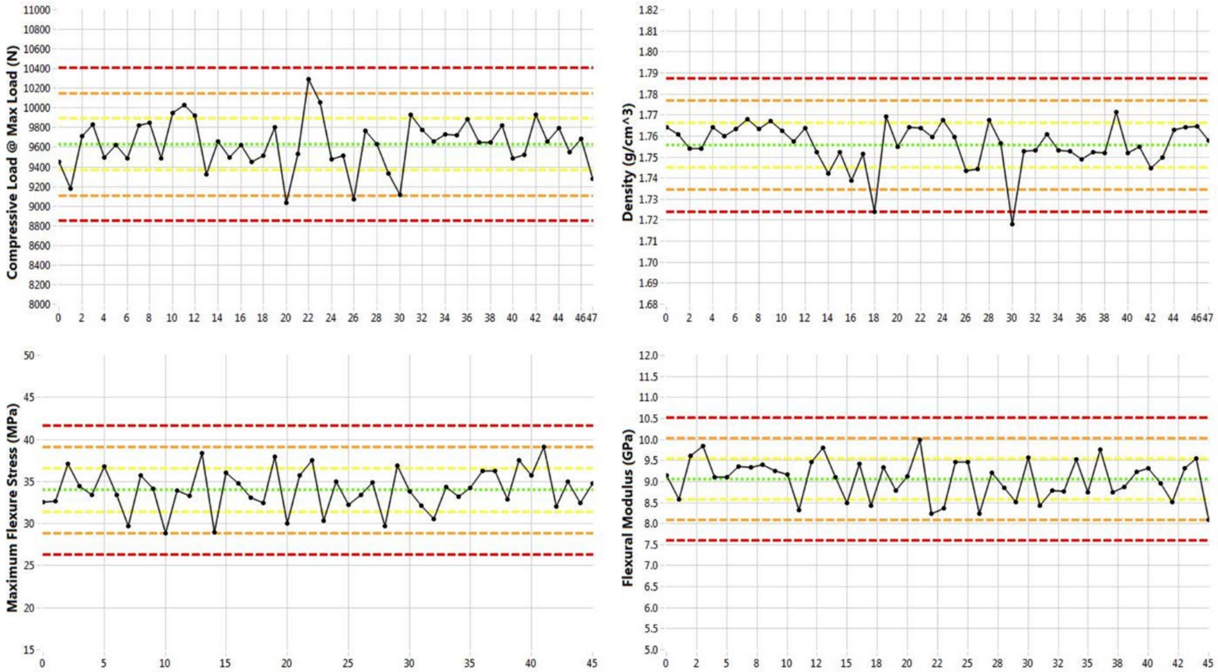

Figure 25. Example baseline data from the unirradiated baseline material property testing.

2.3.1.2 Mechanical Testing of Graphite—Diametral Compression Test Development.

Material irradiation experiments like the advanced graphite creep (AGC) experiment are complicated and have limitations. These experiments seek to investigate the response of material properties of different graphite types to irradiation temperature, dose, and stress condition. The large number of variables combined with limited capsule space typically results in small specimen sizes. Understanding the effects of these geometric limitations on the property measurement techniques is crucial.

Compressive and flexural strength are relatively straight forward to measure on small specimen sizes, while tensile strength is not. Understanding how tensile strength changes with the irradiation conditions is key to the design and safe operation of high-temperature gas and molten salt reactors. In the AGC Baseline Program tensile strength of unirradiated graphite is measured using ASTM C749, “Standard Test Method for Tensile Stress-Strain of Carbon and Graphite.” In this test, hour-glass specimens are machined and uniaxially tested in tension. These specimens are 1 to 2 cm in diameter and 10 to 20 cm in length. Because they are extracted from full billets of each particular graphite type, their size is of no consequence; however, this size specimen in an irradiation experiment would be a very inefficient use of space. Originally, the project planned to use a glued-end tensile test that attempted to use high-strength epoxy to fasten connection adaptors to the ends of AGC specimens for uniaxial testing. Premature adhesive failure and difficulties in alignment resulted in unacceptable levels of uncertainty in obtaining the tensile strength of the AGC irradiated graphite. Two years ago the program began to investigate a technique in which the smaller button specimens are compressed on edge. This diametral compression test results in strain that is transverse to the loading direction ultimately breaking the graphite in tension.

The diametral compression test, also referred to as the Brazilian disk or split disk test, has been used for decades to measure the tensile strength of ceramics, rock, and concrete. This method is being adapted in the AGC Program and has reached a level of maturity that shows it can be used for some graphite types to determine a tensile strength that is closely related to the uniaxial tensile strength of ASTM C749.

Figure 26 shows the average tensile strength obtained using the American Society of Testing and Materials (ASTM) method compared to the results of the diametral compression (split disk) method for four different graphite grades. Good agreement is seen for the medium- to large-grain graphite grades of PCEA, NBG-18, and NBG-17, with the average falling within one standard deviation. Agreement is not as good for the fine grain graphite of IG-110 where almost a 20% difference in average failure stress is shown. Further testing is required to determine the cause of this but at this point it is speculated that in the case of the finer grain more uniform graphites such as IG-110, the critical flaw size from which the fracture initiates is not being captured in the relatively small stressed volume of the split disk test.

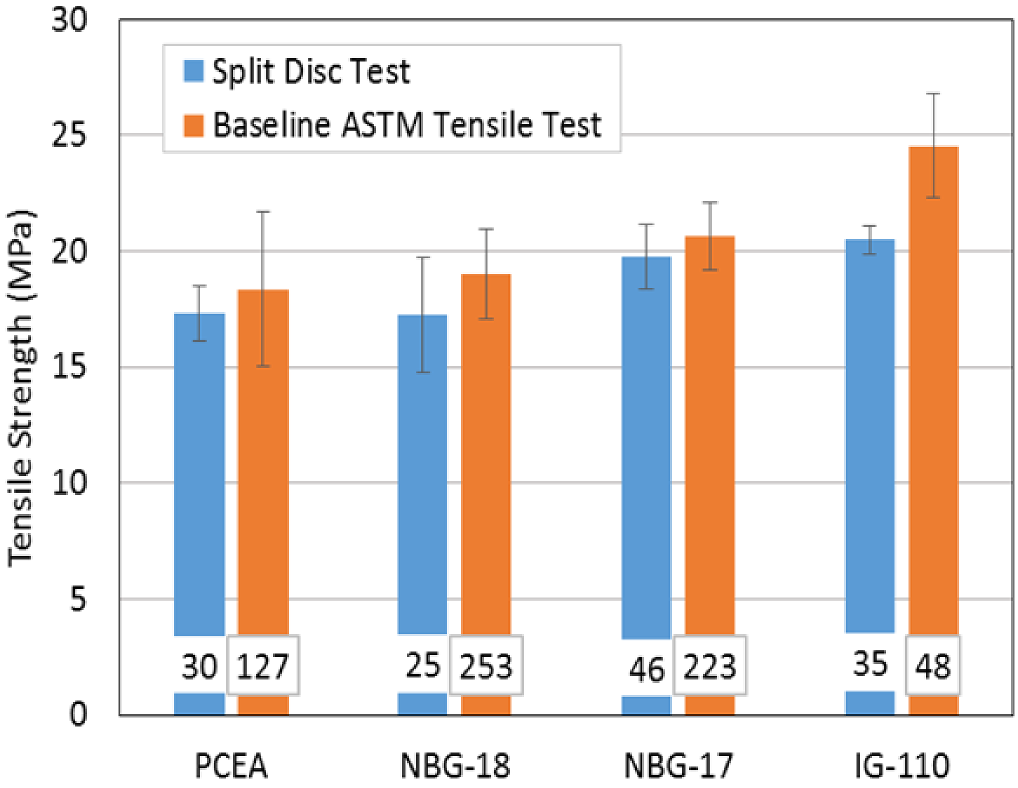

Figure 26. Comparison of diametral compression strength to ASTM C749 tensile strength for four of the major grades of graphite in the AGC irradiation experiments. Error bars represent one standard deviation in the data.

2.3.1.3 Mechanical Testing of Graphite—Development of an ASTM Standard for the Diametral Compression Test. Personnel from the AGC Program continue to make significant contributions to the ASTM DOF.2 Committee on manufactured carbon and graphite products. Focused work in the fourth quarter of FY17 has been on drafting a new standard for the diametral compression test. In particular, INL has taken the lead on performance of the inter-laboratory study (ILS) for this new standard. INL coordinated with seven different national and international laboratories, supplying them with fixtures and specimens for testing (see Figure 27).

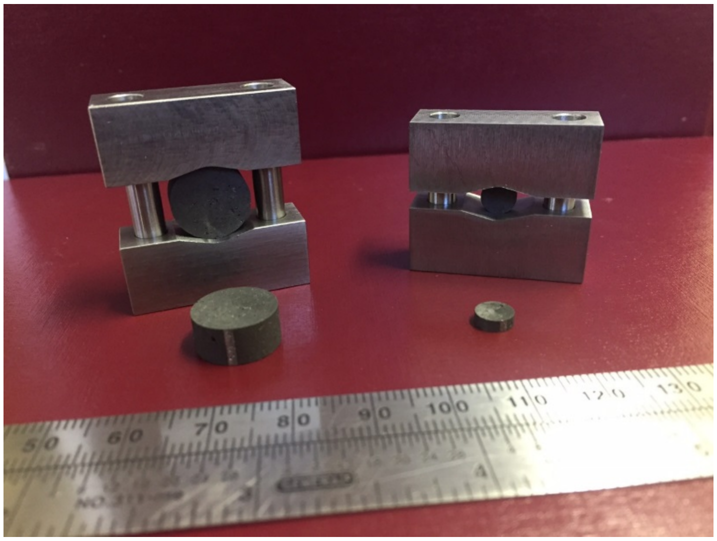

Figure 27. Example of test specimens and fixtures supplied by INL to each participating laboratory.

Data were gathered on two different graphite types and two diameters of disk specimens. Figure 28 and Figure 29 show a summary of the data for two orientations of graphite grade NBG-18 and random orientation of 2114, respectively. In the case of the large-grain NBG-18 graphite, five out of the seven laboratories had reasonable agreement between their diametral compression strength measurements and the uniaxial tensile strength measured under the AGC Baseline Program (dotted line). However, two of the laboratories did not match so well with differences showing up on the smaller-diameter specimens. In the case of the fine grain graphite, 2114, the ILS measured strength values were consistently lower. Again, laboratories number 1 and 2 showed significantly higher values for the smaller-diameter specimens. This data will be submitted to the ILS committee for review and analysis in the first quarter of FY18. Their analysis will result in a precision and bias statement that will be included as part of the new diametral compression test ASTM standard practice.

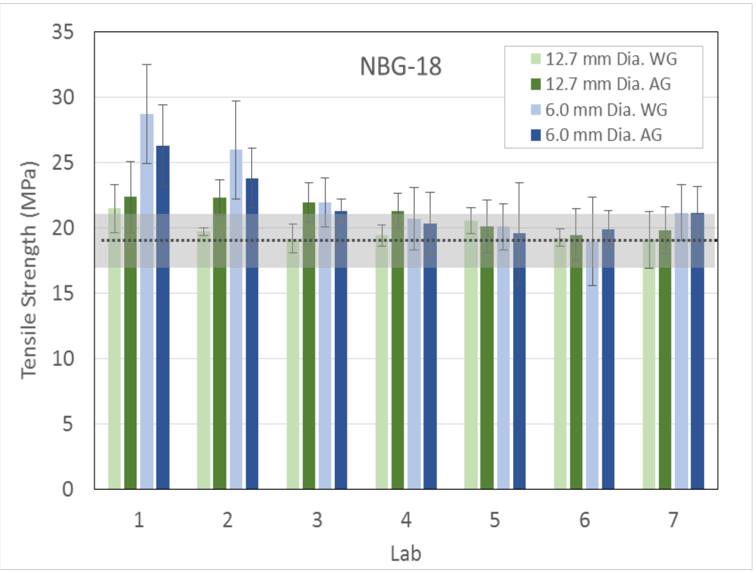

Figure 28. Summary of tensile strength measurements using the draft ASTM standard for seven different laboratories. Data show two different orientations of NBG-18 (with grain, WG, and against grain, AG) compared to uniaxial tensile strength measurements made in accordance with ASTM C749 shown by the dotted line at 19 MPa. Error bars and gray bar represent one standard deviation.

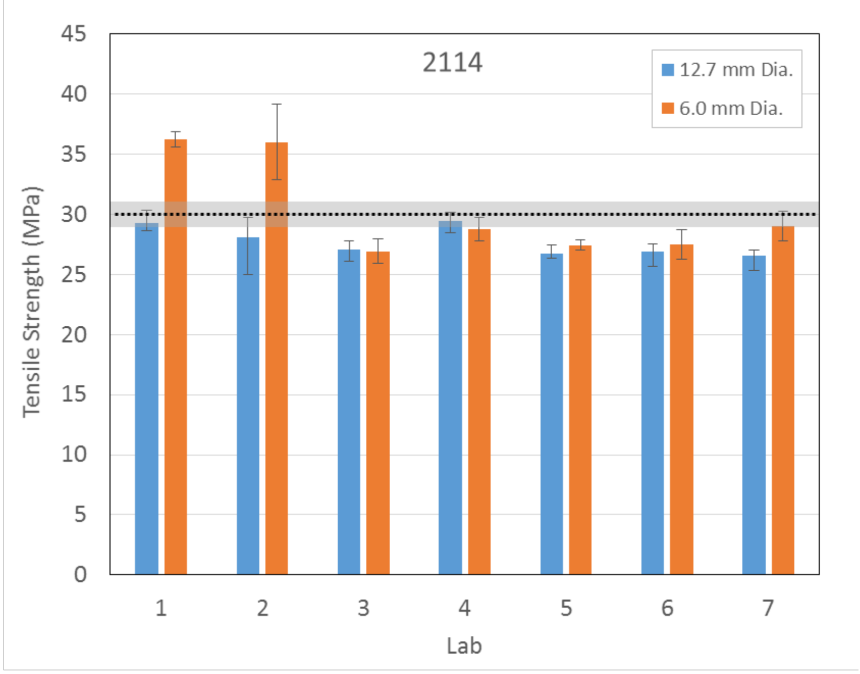

Figure 29. Summary of tensile strength measurements using the draft ASTM standard for seven different laboratories. Data show diametral strength values for graphite grade 2114 compared to uniaxial tensile strength measurements made in accordance with ASTM C749 shown by the dotted line at 30.2 MPa. Error bars and gray bar represent one standard deviation.

2.3.1.4 ASTM Committee Actions. In addition to the diametral compression test development, other ASTM D02.F Committee activities of note during the fourth quarter of FY17 include:

- Completed revisions to ASTM C781, "Standard Practice for Testing Graphite and Boronated Graphite Materials for High-Temperature Gas-Cooled Nuclear Reactor Components." These revisions included adding a section on the determination of specific heat. This standard is considered the starting point for guidance on making nuclear-grade graphite material property measurements (David Swank/Mark Carroll—INL ART-AGC).
- Completed a draft scope for a guide on pore volume measurement techniques (Christian Contescu—ORNL ART-AGC).
- Significant revisions to ASTM C714, "Test Method for Thermal Diffusivity of Carbon and Graphite by Thermal Pulse Method," were made and approved in the main committee balloting process (Dave Swank—INL ART-AGC).
- Nassia Tzelepi of the National Nuclear Laboratory, UK, was elected as the new chairman and Dave Swank of INL, United States of America, was elected as the new secretary.
- Precision and bias statement was completed for the inter-laboratory study of C769 Test Method for Sonic Velocity in Manufactured Carbon and Graphite Materials for Use in Obtaining Young's Modulus (Tim Burchell—ORNL ART-AGC).

2.3.1.5 Chronic Oxidation of Nuclear Graphite, Model Development for Helium with Water Vapor. The activity during July through September 2017 was focused on preparation of a number of specimens oxidized by moisture up to 5 to 6% weight loss for further examination of the effect of temperature on the oxidized layer density profile. The equilibrium penetration depth of the oxidant (water) results from the balance between two opposed processes: oxidant transport in the graphite structure and oxidant consumption by chemical reaction. Both processes depend on temperature, but in different ways. The net effect is that the oxidized layer profile is a strong function of temperature, but this temperature dependence is specific to each grade of graphite. For a complete understanding of these processes, in addition to the knowledge of kinetic parameters, the structure factor of each grade of graphite needs to be determined. The structure factor is the ratio between the effective diffusivity of moisture in a particular graphite grade and the free gas phase diffusivity of moisture in helium, at the same temperature. With the two factors (kinetics and transport) characterized for each graphite grade, the maximum penetration depth and the equilibrium concentration profile of the oxidant as a function of temperature can then be predicted.

The method proposed by Wichner et al. [R.P. Wichner, T.D. Burchell, C.I. Contescu: "Penetration depth and transient oxidation of graphite by oxygen and water vapor", *J. Nucl. Mater.* **393** (2009) 518-521] was used. In general, the density profile in the oxidized layer is expected to follow an exponential decay (from center towards the exposed surface) with decay rates that vary strongly with temperature. Validation of this model requires quantitative characterization of the exponential decay rate of graphite density in the oxidized layer at several temperatures. Optical microscopy is a convenient method to observe density variations in the oxidizer layer. In order to enhance the accuracy, it is preferable to use specimens with a large enough oxidation level, such that the local differences between the oxidized and un-oxidized regions of the graphite specimens can be easily detected. Based on past experience, an oxidation level of 5 to 6% was selected as target for preparation of oxidized specimens for optical microscopy examination.

To reach 5 to 6% weight loss by oxidation in moist helium takes a long time at low temperatures, but low temperature-samples (almost uniformly oxidized) are needed for characterization. Four temperatures were selected: 900, 950, 1000, and 1050°C; continuous runs were performed in helium with 300 Pa H_2O at these temperatures. At this time we completed all four runs with graphite grade 2114 (Mersen) with graphite IG-110 (Toyo Tanso). At the lowest temperature (900°C) reaching up to 5 weight percent mass loss took about 440 hours for graphite 2114 and 260 hours for graphite IG-110. This difference does not reflect substantial variations between the oxidation rates of the two grades. Rather, the longer time needed for grade 2114 reflects the fact that these specimens were larger (about 890 g) than the IG-110 specimens (about 460 g). Table 11 shows specific information on these oxidation runs. Some tests during July and August 2017 were slowed down by the need to resupply the 16 pack of ultra-high purity helium bottles and the pure argon gas; and by the failure of the hygrometer power supply during continuous tests. The hygrometer was also due for periodic maintenance and calibration and was shipped back to the manufacturer for repairs and annual calibration/maintenance.

Table 11. Summary of preparation runs for oxidized by water specimens.

Graphite Grade	Sample ID	Temperature (°C)	Dates		Burnoff (%)	Comments
			From	To		
2114	M-44	950	14-Jun	22-Jun	4.90	—
2114	M-45	1000	26-Jun	29-Jun	5.06	—
2114	M-46	900	30-Jun	29-Jul	5.28	Re-supplied UHP helium and argon
2114	M-47	1050	3-Aug	6-Aug	5.86	—
IG-110	IG-47	900	7-Aug	7-Sep	4.67	Hygrometer shipped out for repairs and calibration
IG-110	IG-48	950	7-Sep	14-Sep	4.98	—
IG-110	IG-49	1000	22-Sep	25-Sep	5.22	—
IG-110	IG-50	1050	25-Sep	26-Sep	5.22	—

2.3.1.6 High-Temperature Vessel Data Analysis. The analysis of high-temperature vessel (HTV) irradiation data was reported at INGSM 2017 in Baltimore, MD. The high-temperature data were obtained to guide the capsule design for the AGC-5 and AGC-6 experiments. The volume change data are shown in Figure 30.

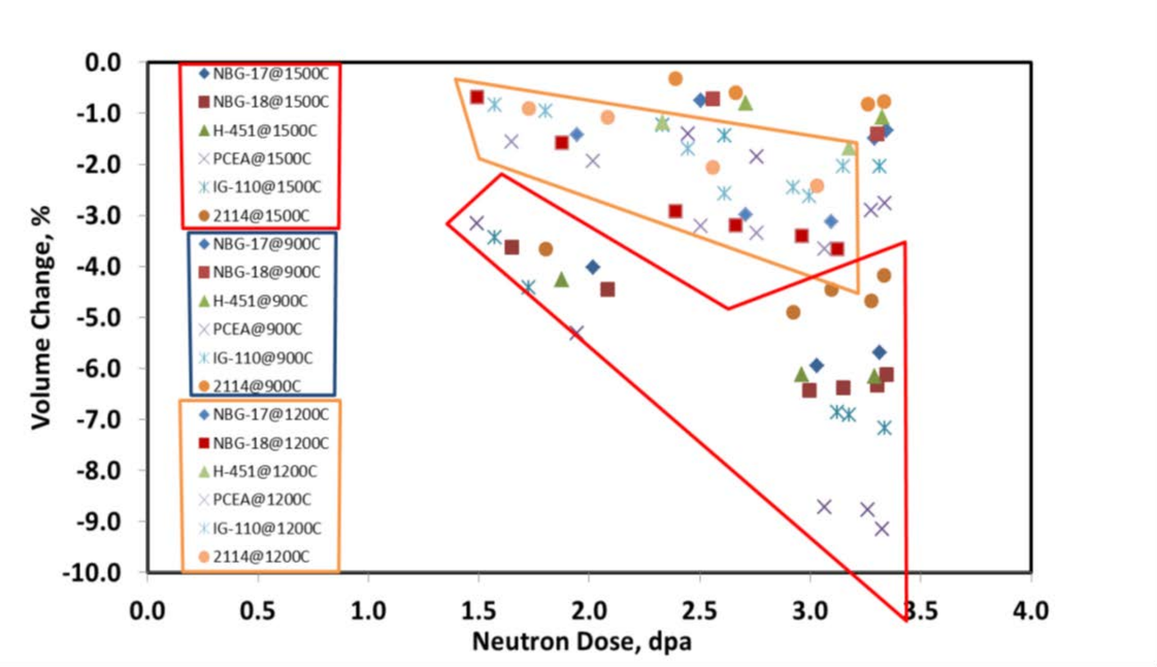

Figure 30. Variation of graphite volume change at high temperature for grades examined in the HTV capsule.

From previous studies the volume turnaround was expected to occur at lower ΔV/V values as the irradiation increases from approximately 300°C to approximately 900°C. The data from the HTV show the opposite trend, as irradiation temperature increases from approximately 900°C to approximately 1500°C the ΔV/V value gets progressively larger in magnitude (from approximately –2.5% to approximately –3% to approximately –9%). The approximately 300°C to approximately 900°C trend is explained by the increasing closure of thermal cracks with temperature that would otherwise accommodate the c-axis expansion allowing the a-axis shrinkage to be more dominant as temperature increases. When this single crystal mechanism is combined with the thermal closure of aligned thermal cracks the lower temperature trend is explainable. However, the increasing ΔV/V change with temperature from approximately 900°Cto approximately 1500°C is purely a function of the increasing crystal growth/shrinkage rate at elevated temperatures (Figure 31).

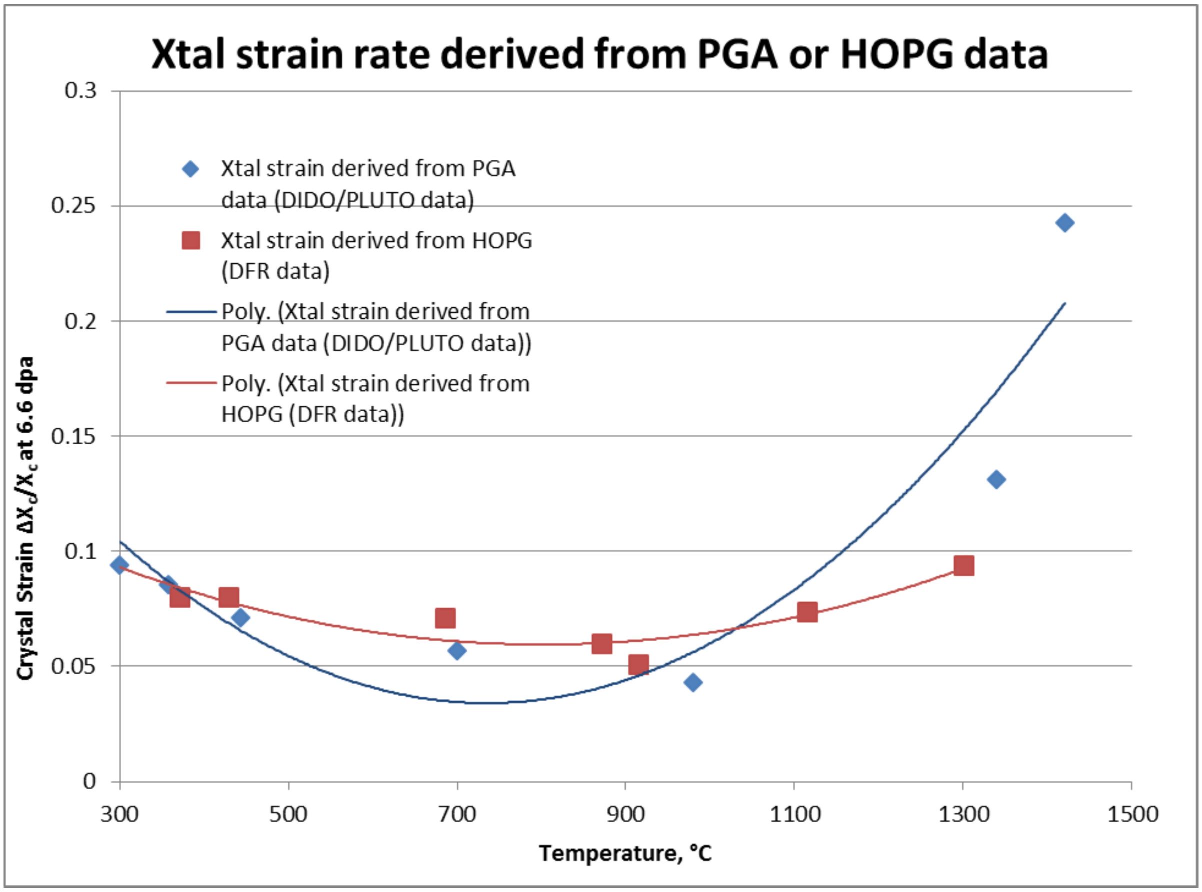

Figure 31. Single crystal growth rates. Replotted from B.T. Kelly, Physics of graphite, Applied Science Publishers, 1981, p. 431.

2.3.1.7 ASME. During the fourth quarter of FY17 a consolidated version of the composite code has been produced and articles of the code have been approved through the appropriate ASME subgroups. The consolidated code has been reviewed prior to final editing and will go to the ASME Section III Committee for approval. The Next Generation Nuclear Plant licensing paper has been reviewed as a basis for the Nuclear Regulatory Commission code/licensing roadmap to be led by Dr. Will Windes.

2.3.1.8 INGSM 2017. The 2017 INGSM was held in Baltimore, MD, September 17–21, 2017. William Windes, Joshua Kane, Timothy Burchell, Nidia Gallego, Anne Campbell, and Diana Russell, chaired, hosted, and coordinated this conference. The event ran quite smoothly and was widely acknowledged as an improvement upon the successes of previous INGSM events. Windes, Kane, David

Swank, Michael Davenport, Paul Humrickhouse, and Rebecca Smith presented the wide range of graphite-related work under way at INL. Burchell, Gallego, Campbell, Lou Qualls, Yoonjo Lee, and Cristian Contescu presented ongoing graphite-related work at ORNL. Topics ranged from irradiation experiments and mechanical testing to inspection and monitoring, and from oxidation behavior and microstructural characterization to theory and modeling. INGSM 2017 provided an outstanding forum of graphite manufacturers, nuclear regulators, reactor developers, and researchers for discussion of ongoing research activities, collaboration in areas of mutual interest, and identification of the greatest needs for future work worldwide. Participation enhanced the influence and reputation of the INL Materials Science and Engineering Department and the ART R&D Program for progress at the forefront of materials research in support of nuclear applications.

Presenters and titles included:

- W. David Swank—Graphite tensile strength results using the diametral compression test
- Lou Qualls—Material needs for Molten Salt Reactors (Keynote Talk)
- Anne Campbell—Measuring microstructure changes in irradiated nuclear graphite
- Cristian Contescu—Mesopore development in irradiated graphite
- Timothy Burchell—Dimensional and modulus changes in HTR relevant graphites at elevated irradiation temperatures
- William Windes—Dimensional and material property changes in nuclear grade graphite during thermal creep
- W. David Swank—An evaluation of AGC Pre and Post irradiation properties
- Joshua Kane—Modelling nuclear graphite oxidation intrinsically
- Joshua Kane—Oxidation behaviors of NBG-18 and NBG-25 nuclear graphite
- Yoonjo Lee—Chronic oxidation of Mersen 2114 fine-grained nuclear graphite by water vapor in normal HTGR operations
- Rebecca Smith—Oxidation performance of graphite samples in thermogravimetric analyzer versus vertical furnace
- Michael Davenport—Advanced Graphite Capsule (AGC) Irradiation status in ATR
- Paul Humrickhouse—Reactor dosimetery and uncertainty quantification in support of the Advanced Graphite Creep (AGC) Experiments.

Also, several posters were presented:

- ORNL High Flux Isotope Reactor (HFIR) Capabilities and Accessibility (Campbell, Bryan, Hirtz, and Tirrani)
- Low Activation Materials Development and Analysis (LAMDA) Laboratory: Capabilities for Measuring Irradiated Materials Properties and Microstructure (Campbell, Schmidlin, Parish, Edmondson, Leonard, Katoh, and Terrani)
- GEN-IV Materials Handbook (Lin, Ren, and Gallego)
- INL Graphite and Materials Research (Windes, Smith, Kane, Swank, and Matthews)
- INL Advanced Test Reactor (Utterbeck, Pepin, Lillo, and Windes).

2.4 Methods

2.4.1 Experiments and Computational Fluid Dynamics Validation

2.4.1.1 High Temperature Test Facility. The test acceptance report for OSU HTTF Test PG-22 was issued. This test was a gas exchange between the primary coolant system and the reactor cavity simulation tank, with a 125°C maximum coolant temperature rise across the core. Data from the test were transmitted to INL.

Core disassembly to investigate the cause of the heater rod failures revealed indications of melted ceramic and graphite sublimation. The working theory is that the contact between adjacent rodlets was reduced as the stacks of heater rods shifted laterally, resulting in smaller contact areas between rodlets, which in turn led to electrical arcing and very high local temperatures. The heater rodlet damage is consistent with damage the graphite program has seen from electrical arcing. Redesigned rodlets have been proposed that are twice as long (fewer interfaces between rodlets), have a ball and hemisphere design rather than a beveled connection (more contact area, accommodates radial movement), and are narrower in the middle (should produce more uniform axial heating). The plan is to perform benchtop tests first, followed by in-vessel tests of some heaters, then followed by full-core replacement (assuming each previous testing step is successful). Besides the heater rodlets, major efforts include reforming four of the core blocks and replacing the leads to the Type-C thermocouples in the core, none of which were working for the matrix tests. Obtaining commercial heater rods to replace the stacks of graphite rodlets was also considered, but would require a redesign of the upper plenum and outer reflector blocks, and would result in a significant reduction (by more than 600°C) in the peak operating temperature of the facility. Total cost estimates are about $380,000 for the graphite rodlet option and $350,000 for the commercial heater rods; common costs for the core blocks and thermocouples are about $120,000.

The RELAP5-3D code was assessed using data from Test PG-22. Both the heatup from ambient and the gas exchange phases of the test were simulated. The code calculations did not predict the reverse natural circulation flow through the core and hot and cold ducts that occurred in the test after about 8 hours. The indications are that the core stored energy was underpredicted, but there were no core temperature data with which to compare. The heater power and coolant flow rate during initial heatup were also unknown. The principal conclusion of the analysis was that the data are insufficient for code assessment.

2.4.2 Physics Methods

An accurate, high-resolution full-core model of prismatic high-temperature reactors for burnup and transient analysis remains a challenge for both reactor analysts and computer codes. The cores are spatially large, but some features are quite small (TRISO particles, burnable poison [BP] pellets). The treatment of both neutron scattering in graphite and resonance capture are complex and not adequately captured using the methods traditionally used in HTGRs and commonly used in light-water reactors (LWRs). For transient analysis, temperature feedback is a function of the TRISO fuel form, but full-core models cannot resolve phenomena at this scale without careful averaging over space and energy. For burnup calculations, a second (pin) level of heterogeneity must be resolved to capture the local effects of BPs and fuel pins while accurately propagating their effects through and between blocks.

The OECD MHTGR Benchmark is being used at INL to drive the development of full-core and transient models and for code-to-code verification against other methods. The IAEA CRP on HTGR Uncertainty Analysis in Modeling is likewise being developed to compare the propagation of uncertainties in lattice and full-core modeling. The tools developed in these activities are being used in related HTGR support work, for example in the joint modeling of the high-temperature test reactor with the Japan Atomic Energy Agency under the ART Civil Nuclear Energy Research and Development Working Group funding. Existing lattice tools (e.g., DRAGON, HELIOIS, SERPENT, and SCALE) have different strengths and weaknesses, and concurrent modeling with these tools helps to identify code and model discrepancies, sensitivities, and best practices.

2.4.2.1 OECD/NEA MHTGR-350 Benchmark. INL is leading an international prismatic HTGR benchmark for comparing and evaluating lattice and core analysis codes, based on the 350-MW MHTGR design information obtained from General Atomics (GA). Similar to the PBMR-400 Transient Benchmark sponsored by the OECD NEA, this OECD/NEA benchmark is a multiyear (2013–2018) project that has already yielded a set of reference steady-state and lattice problems that can be used by DOE, the Nuclear Regulatory Commission, and vendors to assess their codes. The OECD/NEA sponsorship of the prismatic benchmark is valuable since it attracted international participation and leveraged benchmark expertise and publishing apparatus already used for other LWR, sodium fast reactor, and high-temperature reactor development programs.

This benchmark activity is now being completed with the data submitted for Phases I and III currently being compared. The comparisons of Exercise 2 of Phase I, as well as the results for Phase III, will be completed by the end of December 2017 and released to the OECD and DOE as a Level 3 milestone report. The scheduled milestone date of August 31, 2017, was postponed due to the participants' data being received later than planned and the INL's principle investigator's involvement with the simulation of the Transient Reactor Test facility.

2.4.2.2 IAEA CRP on HTGR Uncertainties.

2.4.2.3 In many cases, best estimate plus uncertainty analysis of reactors is replacing the traditional conservative (stacked uncertainty) method for safety and licensing analysis. The use of a more fundamental methodology is also consistent with the reliable high-fidelity physics models and robust, efficient, and accurate codes available today. To facilitate uncertainty analysis applications**,** a comprehensive approach and methodology must be developed and applied. HTGRs have their own peculiarities including coated particle design, large graphite quantities, different materials, and high temperatures that require simulation techniques not utilized in LWR analysis. The IAEA launched the CRP on the HTGR Uncertainty Analysis in Modeling in 2013 to study uncertainty propagation in the HTGR analysis chain. Two benchmark problems are defined, with the prismatic design represented by the GA MHTGR-350 and a 250-MW modular pebble bed design similar to the HTR-Pebble Bed Module (PM) (INET, China). INL is leading the prismatic reactor problem specification of Phases I through III. The IAEA recently approved an extension of this CRP to September 2019.

A Level 3 milestone report (Strydom and Bostelmann 2017) was submitted at the end of August 2017 on the comparison results obtained for Phase I of the prismatic reactor design cases, based on the 350-MW GA MHTGR. Phase I includes the data sets received for the neutronics cell (Exercise I-1), lattice (Exercise I-2a, b), and supercell (Exercise I-2c) exercises; steady-state (Exercise I-3) and transient (Exercise I-4) thermal fluids exercises; and experimental validation case based on the VHTRC facility.

The majority of the submissions received to date have been for the first two exercises, and focused almost exclusively on the uncertainty and sensitivity quantification of cross-section input uncertainties. None of the participants have yet attempted to quantify the effect of manufacturing data input uncertainties. The two thermal-fluid-until-cell exercises have only been performed by INL, while the VHTRC experimental validation was a joint exercise by GRS and INL. The data received for Phase I and, consequently, the focus of this report are mostly on the prismatic HTGR neutronics.

In general, it was found that cross-section uncertainties lead to 550 to 600 pcm one-sigma variations in the cell, block, and supercell eigenvalues. In a separate assessment of user, method, and modeling uncertainties (using best-estimate values without cross-section uncertainties) it was found that differences in the treatment of Doppler broadening, BPs, and the double heterogeneity (DH) nature of the TRISO fuel lead to significant differences of up to 1500 pcm between participants' data sets. These differences can be seen as code- and/or user-specific biases (i.e., it is not stochastic in nature). No specific trends were identified in terms of Monte Carlo or deterministic uncertainty methods. Both methods obtained similar uncertainty results.

The researchers listed below submitted results for the Phase I exercises. A summary of the methods, codes, and nuclear data libraries used by the participants is shown in Table 12 and matched to the exercise submissions received in Table 13 and Table 14.

- Gesellschaft für Anlagen- und Reaktorsicherheit (GRS), Germany—F. Bostelmann, Dr. W. Zwermann
- IAEA, Austria—H. Kim, F. Reitsma
- INL, United States of America—G. Strydom
- National Research Center "Kurchatov Institute" (KI), Russia—Dr. V. Boyariniv, A. Grol
- Korea Atomic Energy Research Institute (KAERI), South Korea—Dr. T-Y Han
- North West University (NWU), South Africa—S. Sihlangu, V. Naicker.

Table 12. Overview of the Phase I transport and U/S codes, as well as the nuclear cross-section data and covariance libraries used for the uncertainty and sensitivity analysis (U/SA).

Participant	U/S Method	U/S Code	Transport Code	ENDF/B-VII.0 Data	ENDF/B-VII.1 Data
GRS	Random sampling	XSUSA	SCALE 6.1.2/ NEWT	238g xs data, 44g cov. data	—
GRS	Perturbation theory	SCALE 6.2/ TSUNAMI	SCALE 6.2/ NEWT	238g xs data, 44g cov. data	252g xs data, 56g cov. data
GRS, INL, NWU, IAEA	Random sampling	SCALE 6.2/ SAMPLER	SCALE 6.2/ NEWT	238g xs data, 44g cov. data	252g xs data, 56g cov. data
INL, NWU, IAEA	Perturbation theory	SCALE 6.2/ TSUNAMI	SCALE 6.2/ KENO-VI	CE xs data, 44g cov. data	CE xs data, 56g cov. data
IAEA	Perturbation theory	SCALE 6.2/ TSUNAMI	SCALE 6.1.2/ NEWT (RPT)	238 xs data, 44g cov. data	—
KAERI	Perturbation theory	McCARD	McCARD	CE xs data, 190g cov. data	CE xs data, 190g cov. data
KAERI	Perturbation theory	MUSAD	DeCART	190 xs data, 190g cov. data	190 xs data, 190g cov. data
KI	Perturbation theory	SCALE 6.2/ TSUNAMI	SCALE 6.2/ KENO-VI	238 g xs data, 44g cov. data	252 g xs data, 56g cov. data
KI	Perturbation theory	SUW	WIMS-D5	69 g xs data, SCALE rev05 44g cov. data	69 g xs data, SCALE rev05 44g cov. data

Table 13. Summary of Phase I, Exercises I-1 and I-2, nominal eigenvalues (k-infinity).

Participant	1a_CZP	1a_HFP	1b_CZP	1b_HFP	2a	2b	2c
GRS-INL SERPENT-ENDF71-Random	1.31612	1.18124	1.36899	1.24335	1.05559	0.96126	1.06283
GRS-INL-SCALE62-SAMPLER-NEWT-ENDF70	1.30983	1.17926	1.36448	1.24439	1.05687	0.96503	1.06942
GRS-SCALE62-SAMPLER-NEWT-ENDF71	—	—	1.35926	1.23807	1.05077	0.96336	1.06339
GRS-SCALE62-TSUNAMI-2D-ENDF70	1.30944	1.17894	—	—	—	—	—
GRS-SCALE62-TSUNAMI-2D-ENDF71	1.30811	1.17558	—	—	—	—	—

Participant	1a_CZP	1a_HFP	1b_CZP	1b_HFP	2a	2b	2c
GRS-SCALE612-TSUNAMI-2D-ENDF70	1.30797	1.17968	—	—	—	—	—
GRS-XSUSA-NEWT-ENDF70	1.30813	1.17980	1.36068	1.23997	1.05658	0.96482	1.08937
GRS-SCALE612-TSUNAMI-DH-ENDF70	—	—	1.36144	1.24134	—	—	—
GRS-SCALE612-TSUNAMI-DH-ENDF71	—	—	1.36064	1.23944	—	—	—
KAERI-McCARD-CE-ENDF71-SCALE-COV44	1.31575	1.18124	1.37115	1.24442	1.05407	0.96221	1.06194
KAERI-McCARD-CE-ENDF71	1.31575	1.18124	1.37115	1.24442	1.05525	0.96145	1.06703
KAERI-MUSAD-DECART-190G-ENDF71	1.32002	1.19227	1.36734	1.24957	1.05799	0.96715	1.07320
KAERI-McCARD-CE-ENDF70	1.31585	1.18257	1.37105	1.24577	1.05383	0.96201	1.06169
KAERI-MUSAD-DECART-190G-ENDF70	1.31644	1.18980	1.36792	1.24976	1.05826	0.96747	1.06411
KI-WIMS-SUW-70	1.31855	1.18375	1.37021	1.24512	1.05808	—	—
KI-WIMS-SUW-71	1.31716	1.18274	1.37172	1.24628	1.05922	—	—
KI-TSU-MG	1.30977	1.18155	1.36254	1.24497	1.06611	—	—
KI-TSU-CE	1.31477	1.18215	1.37669	1.25126	1.06650	—	—
INL-TSUNAMI-62-3D-CE-ENDF71	1.31489	1.18201	1.37514	1.25071	1.06101	0.96605	1.06372
INL-TSUNAMI-62-2D-252-ENDF71	1.30849	1.18129	—	—	—	0.96310	1.06468
GRS-INL-SAMPLER-62-NEWT-252-ENDF71	1.30854	1.18234	1.36327	1.24414	—	—	1.06332
NWU-Tsunami-3D-CE-ENDF70	1.31034	1.18294	1.37433	1.25657	1.06416	—	—
NWU-Tsunami-2D-MG-ENDF70	1.31194	1.18325	1.36078	1.24493	1.05781	—	—
Spread (max-min)	*0.01205*	*0.01669*	*0.01743*	*0.01850*	*0.01573*	*0.00602*	*0.02768*
Mean	*1.31272*	*1.18223*	*1.36721*	*1.24562*	*1.05843*	*0.96426*	*1.06744*
Std-dev (abs)	*0.00403*	*0.00367*	*0.00567*	*0.00463*	*0.00447*	*0.00216*	*0.00805*
Std-dev (%)	*0.31*	*0.31*	*0.42*	*0.37*	*0.42*	*0.22*	*0.75*

Table 14. Absolute difference between k-inf values for two cross-section libraries (k$_{\_\mathrm{ENDF7.1}}$-k$_{\_\mathrm{ENDF7.0}}$).

Participant	1a_CZP	1a_HFP	1b_CZP	1b_HFP	2a	2b	2c
GRS-INL-SCALE62-SAMPLER-NEWT	—	—	−0.00521	−0.00632	−0.00610	−0.00167	−0.00603
GRS-SCALE62-TSUNAMI-2D	−0.00132	−0.00336	—	—	—	—	—
KAERI-McCARD-CE	−0.00010	−0.00133	0.00010	−0.00135	0.00142	−0.00056	0.00534
KAERI-MUSAD-DECART-190G	0.00358	0.00247	−0.00058	−0.00019	−0.00027	−0.00032	0.00909
KI-WIMS-SUW	−0.00139	−0.00101	0.00151	0.00116	0.00114	—	—

More detail on the nominal eigenvalue (k-infinity, or k-inf) results submitted for Exercises I-1a, I-1b, and I-2 are provided in Table 13. In addition to the k-inf values, the mean and one standard deviation (std-dev in absolute and relative %) of the data set are shown as an indication of the spread between the participants' results. Following an informal convention in U/SA, individual results that are higher or lower than 2 standard deviations from the mean value (2σ or 5 to 95%) are identified in yellow. The Monte Carlo statistical variances are not shown in these tables for clarity, but all results had population 1σ variances smaller than 25 pcm (i.e., ±0.00025).

A few observations can be made on the data shown in Table 13:

- The use of the ENDF-B-VII.1 library data leads to k-inf values approximately 100 pcm lower than the ENDF-B-VII.0 values. This can be attributed to an underestimation of the carbon neutron capture cross section at thermal energies in the ENDF-B-VII.0 library. The correction of this cross section in ENDF-B-VII.1 resulted in increased neutron capture and thus a reduction in the multiplication factor. This observation is mostly confirmed for this larger data set (marked in Table 14 as green entries), but for nine cases, the ENDF-B-VII.1 values were actually *higher* than the ENDF-B-VII.0 values (marked in blue). The variances across the exercises are striking: for Exercise I-1a_CZP, the McCARD CE results differ only by 10 pcm, while several other cases produced differences of more than 600 pcm.
- The spread between the results obtained for each exercise is defined as the difference between the maximum and minimum values in the data set. It can be expected that the very simple homogeneous fuel unit cell problem (i.e., Exercise I-1) should produce the best matched set of data. The spread for this case is surprisingly large (e.g., 1205 pcm), and as additional physics-based requirements are added (e.g., Doppler broadening for HFP conditions, DH treatment, BPs), the spread increases (e.g., up to 2768 pcm for Exercise I-2c). The depleted single block Exercise I-2b is, however, an exception to this trend; it is in fact the best-matched Phase I result (602 pcm spread) with the lowest standard deviation as well. The addition of BPs to the fresh block problem clearly caused larger differences (1573 pcm spread and 1σ = 447 pcm). The representation of the BP compacts is therefore an important component of modeling (or user choice) uncertainties in the Phase I models.
- With the exception of four cases, all results are within 2σ of the respective mean values for a particular exercise. The standard deviations of the results provided for each of these exercises vary between 216 pcm for Exercise I-2b to 805 pcm for Exercise I-2c. The higher values of the two KAERI 190-g DeCART solutions for Exercise I-1a-HFP can probably be related to a Doppler broadening reaction correction method that differs from the other participants (i.e., the values for the Exercise I-CZP variants with the same code is close to the mean value). The NWU and GRS results for Exercise I-1b-HFP and I-2c, respectively, could be examples of incomplete spatial convergence or loose solver settings that can possibly be improved by the participants.
- The addition of an important HTGR simulation complexity (DH fuel) in the Exercise I-1b models produced higher variances between the submitted results, as expected, but it only accounted for an additional 100 to 150 pcm compared to the homogenized fuel case variances. By comparing the results for Exercises I-1a and I-1b, the worth of this DH treatment can be determined. It is shown in Table 15 that the DH worth in general shows reasonable agreement between the participants (5.15 to 6.40%), although it could be argued that more than 1000 pcm is a significant difference for the implementation of this treatment into the various codes. It is in fact comparable to twice the 1σ cross-section uncertainty identified in Table 16. It is also interesting to note that the mean DH worth of the HFP exercise is 900 pcm higher (6.36%) than the CZP mean (5.46%), which suggests that it is even more important to account for the self-shielding effect of this fuel form at the higher fuel temperatures typical of HTGRs.
- The temperature worth of Exercises I-1a and I-1b is also included in Table 15 (i.e., the k-inf difference between the hot and cold cases). This allows comparison of the Doppler broadening reaction correction treatments (or lack thereof) used by the participants, for example. The differences vary between approximately 850 pcm for the homogenous case to more than 1000 pcm for the heterogeneous case (i.e., between one and two times as large as the 1σ cross-section uncertainty). Apart from the cross-section uncertainties, these two modeling uncertainties (accounting for higher

temperatures and the DH nature of the fuel) are significant contributors to the overall simulation uncertainty.

Table 15. Temperature and double heterogeneity worths (%) for Exercises I-1a and I-1b.

Participant	Temperature Worth (%)		Double Heterogeneity Worth (%)	
	1a	1b	CZP	HFP
INL/GRS SERPENT-ENDF71-Random	−13.49	−12.56	5.29	6.21
GRS-INL-SCALE62-SAMPLER-NEWT-ENDF70	−13.06	−12.01	5.46	6.51
GRS-SCALE62-SAMPLER-NEWT-ENDF71	—	−12.12	—	—
GRS-SCALE62-TSUNAMI-2D-ENDF70	−13.05	—	—	—
GRS-SCALE62-TSUNAMI-2D-ENDF71	−13.25	—	—	—
GRS-SCALE612-TSUNAMI-2D-ENDF70	−12.83	—	—	—
GRS-XSUSA-NEWT-ENDF70	−12.83	−12.07	5.26	6.02
GRS-SCALE612-TSUNAMI-DH-ENDF70	—	−12.01	—	—
GRS-SCALE612-TSUNAMI-DH-ENDF71	—	−12.12	—	—
KAERI-McCARD-CE-ENDF71-SCALE-COV44	−13.45	−12.67	5.54	6.32
KAERI-McCARD-CE-ENDF71	−13.45	−12.67	5.54	6.32
KAERI-MUSAD-DECART-190G-ENDF71	−12.78	−11.78	4.73	5.73
KAERI-McCARD-CE-ENDF70	−13.33	−12.53	5.52	6.32
KAERI-MUSAD-DECART-190G-ENDF70	−12.66	−11.82	5.15	6.00
KI-WIMS-SUW-70	−13.48	−12.51	5.17	6.14
KI-WIMS-SUW-71	−13.44	−12.54	5.46	6.35
KI-TSU-MG	−12.82	−11.76	5.28	6.34
KI-TSU-CE	−13.26	−12.54	6.19	6.91
INL-TSUNAMI-62-3D-CE-ENDF71	−13.29	−12.44	6.03	6.87
INL-TSUNAMI-62-2D-252-ENDF71	−12.72	—	—	—
GRS-INL-SAMPLER-62-NEWT-252-ENDF71	−12.62	−11.91	5.47	6.18
NWU-Tsunami-3D-CE-ENDF70	−12.74	−11.78	6.40	7.36
NWU-Tsunami-2D-MG-ENDF70	−12.87	−11.58	4.88	6.17
Mean	*−13.07*	*−12.18*	*5.46*	*6.36*

The mean k-infinity 1σ variances shown in Table 16 range between 550 to 636 pcm for the Phase I exercises (i.e., *the input uncertainties present in the cross-section data lead to 1σ k-inf uncertainties of up to approximately 600 pcm*). This significant uncertainty can be compared with Monte Carlo codes that are typically converged down to 20 pcm or less in production runs, or a difference between two transport codes of less than approximately 100 pcm that is usually seen as acceptable. The CZP uncertainties are consistently lower than the HFP uncertainties.

Table 16. Summary of Phase I, Exercises I-1 and I-2, k-infinity 1σ variances (%).

Participant	1a_CZP	1a_HFP	1b_CZP	1b_HFP	2a	2b	2c
GRS-INL-SCALE62-SAMPLER-NEWT-ENDF70	0.508	0.557	0.489	0.526	0.459	0.661	0.474
GRS-SCALE62-SAMPLER-NEWT-ENDF71	—	—	0.555	0.695	0.459	0.530	0.442
GRS-SCALE62-TSUNAMI-2D-ENDF70	0.527	0.581	—	—	—	—	—
GRS-SCALE62-TSUNAMI-2D-ENDF71	0.530	0.563	—	—	—	—	—
GRS-SCALE612-TSUNAMI-2D-ENDF70	0.528	0.580	—	—	—	—	—
GRS-XSUSA-NEWT-ENDF70	0.544	0.598	0.532	0.585	0.497	0.687	0.482
GRS-SCALE612-TSUNAMI-DH-ENDF70	—	—	0.518	0.569	—	—	—
GRS-SCALE612-TSUNAMI-DH-ENDF71	—	—	0.526	0.559	—	—	—
KAERI-McCARD-CE-ENDF71-SCALE-COV44	0.512	0.556	0.494	0.528	0.462	0.646	0.483
KAERI-McCARD-CE-ENDF71	0.768	0.811	0.753	0.784	0.736	0.540	0.601
KAERI-MUSAD-DECART-190G-ENDF71	0.841	0.919	0.819	0.888	0.800	0.629	0.655
KAERI-McCARD-CE-ENDF70	0.769	0.811	0.752	0.783	0.735	0.542	0.604
KAERI-MUSAD-DECART-190G-ENDF70	0.843	0.921	0.818	0.887	0.803	0.639	0.660
KI-WIMS-SUW-70	0.483	0.564	0.456	0.527	0.424	—	—
KI-WIMS-SUW-71	0.483	0.564	0.456	0.527	0.424	—	—
KI-TSU-MG	0.547	0.589	0.536	0.568	0.515	—	—-
KI-TSU-CE	—	—	—	—	—	—	—
INL-TSUNAMI-62-3D-CE-ENDF71	0.528	0.557	0.512	0.533	0.502	0.544	-
INL-TSUNAMI-62-2D-252-ENDF71	0.543	0.568	—	—	—	—	—
GRS-INL-SAMPLER-62-NEWT-252-ENDF71	0.525	0.556	0.515	0.543	—	—	—
NWU-Tsunami-3D-CE-ENDF70	0.526	0.579	0.520	0.544	0.501	—	—
NWU-Tsunami-2D-MG-ENDF70	0.526	0.578	0.515	0.543	0.501	—	—
Mean	*0.585*	*0.636*	*0.574*	*0.623*	*0.558*	*0.602*	*0.550*
Std-dev (abs)	*0.124*	*0.129*	*0.124*	*0.130*	*0.142*	*0.062*	*0.089*
Std-dev (%)	*21*	*20*	*22*	*21*	*25*	*10*	*16*

The mean k-infinity 1σ variances shown in Table 16 range between 550 to 636 pcm for the Phase I exercises (i.e., *the input uncertainties present in the cross-section data lead to 1σ k-inf uncertainties of up to approximately 600 pcm*). This significant uncertainty can be compared with Monte Carlo codes that are typically converged down to 20 pcm or less in production runs, or a difference between two transport codes of less than approximately 100 pcm that is usually seen as acceptable. The CZP uncertainties are consistently lower than the HFP uncertainties.

For the deterministic General Perturbation Theory method (used in SCALE/Tsunami and the MUSAD code), this variance is determined by the adjoint solution of the transport equation. It therefore requires a forward and adjoint solver sweep. The stochastic method, as used in SCALE/SAMPLE, consists of typically a few hundred calculations using the perturbed cross-section input data. The implementation in SAMPLER limits the number of perturbed libraries available to 1,000, based on the covariance database created with the XSUSA code. The k-infinity 1σ variances for SAMPLER are then simply determined by using the standard formulation of the statistical 1σ standard deviation of a sample population.

It should also be noted in Table 16 that although the spread between the participants seems large, it is mainly caused by the significant difference in the KAERI results (marked in yellow). The use of a different 190 group covariance library (compared to the standard 44-g covariance library in SCALE 6.1.2 and 56 g in SCALE 6.2) by both the McCARD and DeCART codes could affect the resonance self-shielding effect for the U-238 capture reaction. The 190-g structure is based on the DeCART (or HELIOS) structure with very differaent group boundaries compared to the SCALE group structure. The difference is clearly shown in the additional calculation submitted by Dr. Han using the standard SCALE 44-g covariance library, which matches very well with the rest of the SCALE-based covariance data set. The KAERI 190-g results for Exercise I-2b (especially for McCARD) also matches very well with the SCALE 44-g covariance results. This exercise contains significant amounts of Pu-239 that has an important absorption reaction in the resonance region, in addition to the harder overall spectrum.

Exercises I-1c and I-1d were added as additional cases at the 2014 research coordination meeting, representing a fuel-to-moderator ratio that is closer to the actual reactor ratio (e.g., Exercises I-1a and I-1b contains too little graphite and have atypical hard spectra for an HTGR application). Only two participants have submitted results for these two cases. The k-inf and 1σ variances are presented in Table 17, and since it is such a small dataset, only the mean values are calculated. The IAEA submission is the only result received that uses the reactivity-equivalent physical transformation (RPT) method of transforming a DH fuel region into a reduced radius single homogenized fuel region with a matching eigenvalue. The eigenvalue obtained is significantly higher (by more than 950 pcm) than the SCALE/NEWT results submitted by GRS also using the older version of SCALE 6.1.2. The k-inf uncertainty values determined by two different methods (e.g., Tsunami General Perturbation Theory and XSUSA stochastic) compare well within the 504 to 551 pcm range and are slightly lower, but comparable to the Exercise I-1a and I-1b results. The addition of more graphite and the softer spectrum therefore did not influence the impact of the cross-section data uncertainties much (even if the nominal k-inf values between Exercises I-1a and I-1c, for example, differ by more than 4000 pcm).

Table 17. Summary of Phase I, Exercises I-1c and I-1d, nominal eigenvalues and 1σ (%).

Participant	1c_CZP		1c_HFP		1d_CZP		1d_HFP	
	k	1σ (%)	k	1σ (%)	k	1σ (%)	k	1σ (%)
IAEA-SCALE6.1.2-Tsunami-RPT-238g-ENDF70	1.37474	—	—	—	1.42455	—	—	—
GRS-SCALE612-TSUNAMI-DH-ENDF70	1.36501	0.5073	1.24018	0.5565	1.41961	0.4957	1.30303	0.5439
GRS-SCALE612-TSUNAMI-DH-ENDF71	1.36300	0.5208	1.23792	0.5499	1.41812	0.5143	1.30029	0.5440
GRS-SCALE612-XSUSA-ENDF70	1.36501	0.5177	1.24018	0.5680	1.41961	0.5055	1.30303	0.5540
GRS-SCALE612-XSUSA-ENDF71	1.36300	0.5073	1.23792	0.5315	1.41812	0.5012	1.30029	0.5261
Mean	*1.36615*	*0.513*	*1.23905*	*0.551*	*1.42000*	*0.504*	*1.30166*	*0.542*

References

Strydom, G., and F. Bostelmann, 2017, *IAEA Coordinated Research Project on HTGR Uncertainties in Modeling: Comparison of Phase I Nominal, Uncertainty, and Sensitivity Results,* INL/LTD-16-40699, Idaho National Laboratory, August 2017.

3. 90-DAY LOOK AHEAD

3.1 Important Activities

3.1.1 Fuels Development

- Statement of work will be put in place for the equipment and materials disposition activities at BWXT.
- Disposition of waste and unused chemicals at BWXT will commence.
- Planning for equipment dispositioning will be finalized.
- NDMAS has a Level 2 milestone task due December 15, 2017, to publish the AGR-5/6/7 Irradiation Monitoring website.
- Perform FACS heating test of AGR-3/4 Compact 10-2.
- Complete analysis of reirradiated and heating-tested cracked kernels from AGR-2 Compact 6-4-1 and FACS condensate plates exchanged during the heating test.
- Initiate basic optical microscopy on AGR-2 multi-particle mounts from particles received from ORNL.
- Initiate basic optical microscopy on select AGR-3/4 compacts cross sections.
- Complete fission product inventory analysis on AGR-3/4 Capsule 3 and 7 graphite samples at PNNL.
- Initiate analysis on AGR-3/4 Capsule 5 and 8 graphite samples at PNNL.
- Receive shipping containers back from PNNL to support future shipments of AGR-3/4 graphite sample shipments.
- Complete analysis on AGR-3/4 Compact 12-1 and 12-3 radial and axial deconsolidation solutions.
- Complete preparations for shipment of AGR-3/4 Compact 3-3 radial and axial deconsolidation solutions and particles to PNNL.
- Complete preparations for Cell 5 window repairs in the Analytical Laboratory.
- Initiate testing of surrogate materials using the benchtop furnace at IDEF-W4.
- Submit INL external report *Advanced Microscopy Examination on Particle AGR2-223-RS06* for internal review (I. J. van Rooyen, S. Meher, T. Lillo, and K. Wright).
- Continue data collection on lamellae from Location B of Particle AGR2-222-RS036.

3.1.2 High-Temperature Materials

- None provided.

3.1.3 Graphite Development and Qualification

- Review and update the content of the IAEA Nuclear Graphite Knowledge Base at the Technical Meeting on the Status of the IAEA Nuclear Graphite Knowledge Base, November 2-3, 2017 in Vienna, Austria (traveler, N. Gallego). The agenda will include the establishment of new terms of reference and membership, efforts to ‘populate’ the knowledge base further, review and improvement of the taxonomy to support the knowledge base, review of the progress achieved in the knowledge base since the last meeting, and the organization of a collective quality assurance exercise for new information and graphite data as appropriate.
- Initiate oxidation profile characterization of slowly oxidized graphite specimens (2114 and IG-110).

- Analyze results of water vapor transport measurements through thin graphite slabs by an outside contractor (Porous Materials Inc., Ithaca, NY).
- Draft methodological guidance for using nitrogen adsorption at 77 K and calculation of Brunauer-Emmett-Teller (BET) surface area of graphite specimens; will submit to ASTM Subcommittee D02F.
- Investigate the possibility of using high-resolution gas adsorption isotherms (nitrogen, argon, and krypton) for characterization of ordered/disordered surfaces in open graphite pores and quantification of the basal plane participation in the total surface area measured by Brunauer-Emmett-Teller (BET) technique.
- Attend the ASME Code Meeting, in October or November 2017, in Phoenix, AZ (ORNL Graphite team staff).

3.1.4 Methods

- Perform separate effects testing with redesigned OSU HTTF heater rods.
- Prepare test acceptance reports for the completed OSU HTTF matrix and shakedown/characterization tests.
- Update RELAP5-3D input model for OSU HTTF based on characterization test data.
- Release the Level 3 milestone report on comparisons of the results submitted for Phases I and III of the OECD/NEA MHTGR-350 Benchmark (due January 5, 2018).